BRNO UNIVERSITY OF TECHNOLOGY
VYSOKÉ UČENÍ TECHNICKÉ V BRNĚ

CENTRAL EUROPEAN INSTITUTE OF TECHNOLOGY BUT
STŘEDOEVROPSKÝ TECHNOLOGICKÝ INSTITUT VUT

ELECTRON MICROSCOPY AND SPECTROSCOPY IN PLASMONICS

ELEKTRONOVÁ MIKROSKOPIE A SPEKTROSKOPIE V PLAZMONICE

SHORT VERSION OF DOCTORAL THESIS
TEZE DIZERTAČNÍ PRÁCE

AUTHOR
AUTOR PRÁCE
Ing. Michal Horák

SUPERVISOR
ŠKOLITEL
prof. RNDr. Tomáš Šikola, CSc.

BRNO 2019

Abstract

This thesis deals with electron and ion beam techniques for fabrication and characterization of plasmonic nanostructures. Analytical electron microscopy focusing on applications in the field of plasmonics is discussed. The emphasis is given to electron energy loss spectroscopy (EELS) and cathodoluminescence. Further, fabrication of plasmonic samples for transmission electron microscopy is introduced while the aim is put at focused ion beam lithography and at sample preparation using chemically synthesized particles in water solution. The main research results are divided into four parts.

The first part covers a comparative study of plasmonic antennas fabricated by electron beam and focused ion beam lithography. While both techniques are suitable for the fabrication of plasmonic antennas, electron beam lithography shall be prioritized over focused ion beam lithography due to better quality of the resulting antennas and considerably stronger plasmonic response in EELS. Antennas fabricated by focused ion beam lithography have slightly dull edges, exhibit pronounced thickness fluctuation, and they are also strongly contaminated not only by organic contaminants, but also by residues of FIB milling including implanted milling ions and atoms of a titanium adhesion layer.

In the second part, Babinet's principle of complementarity for plasmonic nanostructures is investigated on a set of gold disc-shaped antennas and complementary apertures in a gold layer with various diameters. The complementarity is confirmed for fundamental plasmon properties such as resonance energies, but differences rising from the limited validity of Babinet's principle are found, for example, for the spatial distribution of the near-field of plasmon polaritons.

The third part summarizes a study of nanostructures with functional properties related to the local enhancement of electric and magnetic field. Bow-tie and diabolo plasmonic antennas, both in the form of particles and in the form of apertures, exhibit particularly strong local field enhancement. Our study identifies several modes of localized surface plasmons in these antennas and characterizes their properties including mode energy, near field electric and magnetic field distribution, and the qualitative distribution of charge nodes and current associated with electron gas oscillations. Next, we have studied mode energy tunability in near infrared and visible spectral regions and focused on Babinet's complementarity between direct and inverted antennas.

The last part is focused on silver amalgam, which is a novel and very prospective plasmonic material. By changing the size of silver amalgam nanostructures their plasmon resonance can be tuned from ultraviolet through the whole visible to infrared region. As silver amalgam is well investigated in the field of electrochemistry, silver amalgam nanoparticles opens a possibility to combine plasmonics and electrochemistry together.

Key words

Plasmonic antennas, localized surface plasmons, electron microscopy, EELS, cathodoluminescence, Babinet's principle.

HORÁK, Michal. *Electron microscopy and spectroscopy in plasmonics.* Brno, 2019. Available online: https://www.vutbr.cz/en/students/final-thesis/detail/122351. Short version of doctoral thesis. Brno University of Technology, CEITEC BUT. Supervisor of the doctoral thesis prof. RNDr. Tomáš Šikola, CSc.

Abstrakt

Tato práce se zabývá mikroskopickými technikami využívajícími elektronový a iontový svazek pro přípravu a charakterizaci plazmonických nanostruktur. Analytická elektronová mikroskopie je představena se zaměřením na aplikace v oblasti plazmoniky. Důraz je kladen na spektroskopii energiových ztrát elektronů (EELS) a katodoluminiscenci. Dále je diskutována výroba plazmonických vzorků pro transmisní elektronovou mikroskopii, přičemž je kladen důraz na litografii iontovým svazkem a na přípravu vzorků za použití chemicky syntetizovaných částic ve vodném roztoku. Hlavní výzkumné výsledky práce jsou rozděleny do čtyř částí.

První část se věnuje komparativní studii plazmonických antén vyrobených elektronovou a iontovou litografií. Přestože obě techniky jsou vhodné pro výrobu plazmonických antén, elektronová litografie by měla být upřednostňována před iontovou litografií díky lepší kvalitě výsledných antén a jejich silnější plazmonické odezvě. Antény vyrobené iontovou litografií mají neostré okraje, vykazují výrazné kolísání tloušťky a jsou také silně kontaminovány nejen organickými kontaminanty, ale také rezidui po iontové litografii včetně implantovaných iontů z iontového svazku a atomů titanové adhezivní vrstvy.

Ve druhé části je zkoumán Babinetův princip komplementarity pro plazmonické nanostruktury na sérii zlatých diskových antén a komplementárních apertur ve zlaté vrstvě s různými průměry. Komplementarita je potvrzena pro základní plazmonické vlastnosti jako rezonanční energie, ale rozdíly způsobené omezenou platností Babinetova principu jsou patrné například pro prostorové rozložení blízkého pole plazmonových polaritonů.

Třetí část shrnuje studii nanostruktur s funkčními vlastnostmi souvisejícími s lokálním zesílením elektrického a magnetického pole. Obzvlášť silné lokální zesílení pole vykazují plazmonické antény tvaru bowtie a diabolo, a to jak ve formě částic, tak ve formě apertur. Naše studie umožnila identifikovat několik módů lokalizovaných povrchových plazmonů v těchto anténách a charakterizovat jejich vlastnosti včetně energie módu, rozložení elektrické a magnetické složky blízkého pole módu, a kvalitativní rozložení uzlů náboje a proudu souvisejících oscilací elektronového plynu. Dále jsme studovali laditelnost energií módů v blízké infračervené a viditelné spektrální oblasti a zaměřili jsme se na Babinetovskou komplementaritu mezi přímými a invertovanými anténami.

Poslední část je zaměřena na stříbrný amalgám, nový a velmi perspektivní plazmonický materiál. Změnou velikosti stříbrných amalgámových nanostruktur může být jejich plazmonová rezonance laděna od oblasti ultrafialového záření přes celou viditelnou až po infračervenou oblast. Jelikož stříbrný amalgám je dobře prozkoumán v oblasti elektrochemie, stříbrné amalgámové nanočástice otevírají možnost kombinovat plazmoniku a elektrochemii dohromady.

Klíčová slova

Plazmonické antény, lokalizované povrchové plazmony, elektronová mikroskopie, EELS, katodoluminiscence, Babinetův princip.

HORÁK, Michal. *Elektronová mikroskopie a spektroskopie v plazmonice.* Brno, 2019. Dostupné také z: https://www.vutbr.cz/studenti/zav-prace/detail/122351. Teze dizertační práce. Vysoké učení technické v Brně, Středoevropský technologický institut VUT. Vedoucí práce Tomáš Šikola.

Contents

1 Introduction

Interactions of electromagnetic field and free electrons in metals at the metal-dielectric interface are studied in the field of nanophotonics called plasmonics [1]. Plasmonics deals with the generation, manipulation, guiding and transportation of electromagnetic waves in metals based on the interaction between electromagnetic field and collective oscillations of free electrons in metals called plasmons. At the metal-dielectric interface surface plasmon polaritons (SPP) associated with the local electromagnetic field are formed. They were predicted by R. H. Ritchie [2] and experimentally verified by C. J. Powell and J. B. Swan [3] in 1950s and theoretically explained and characterized by A. Otto [4], A. A. Lucas and M. Šunjić [5], and E. Kröger [6, 7] 10 years later. In metallic nanostructures, collective oscillations of free electrons strongly couple to the electromagnetic field forming the excitations called localized surface plasmons (LSP) [8]. The clear mathematical foundation for LSP oscillations was established by G. Mie in 1908 [9]. The first characterization of LSP by electron energy loss spectroscopy was presented by P. Batson in 1982 [10].

A characteristic feature of LSP is a strong enhancement of electromagnetic field within the surrounding dielectric together with its confinement on the subwavelength scale, which can be utilized to control various optical processes in a wide spectral region even below the free space diffraction limit [11]. Significance of this feature is further increased by easy tunability of the optical properties of nanostructures via engineering their size, shape, or dielectric environment [12]. This design flexibility allows creating a large amount of optical functions. Therefore, plasmonic antennas have a wide field of applications [13, 14], for example, in optoelectronics [15], telecommunications [16], photonics [17], microscopy [18], spectroscopy [19], energy harvesting [20], sensing elements [21], and medicine [22]. New discoveries with high application potential are often connected to implementation of new concepts into the field of plasmonics, such as a plasmoelectric effect [23], plasmonic lasing [24], generalized laws of reflection [25], spin-orbit coupling [26], chirality [27], and the Babinet principle of complementarity, which describes the correspondence between optical response of apertures and their complementary particles [28, 29].

Metallic nanostructures supporting LSP resonances can be fabricated using different techniques, such as chemical synthesis [30], optical lithography [31], electron beam lithography [32, 33], focused ion beam milling [34, 35], or 3D nanoprinting [36, 37]. Such nanostructures are often called plasmonic antennas. In most cases, silver or gold is used. Nevertheless, a very prospective material in the ultraviolet and visible range is, for example, aluminum [38, 39, 40]. The quality of prepared plasmonic antennas influences the LSP resonances. These resonances might be affected and degraded by any deviation from an ideal dielectric environment and an ideal shape, for example, by adding an adhesion layer below the antenna [41, 42], by polycrystallinity of the antenna [43, 44], or by surface roughness of the antenna [45, 46].

LSP resonances in plasmonic antennas can be detected using many different tech-

niques, for instance, by dark field optical microscopy [47, 48] or near field optical microscopy [49, 50]. Mapping of LSP resonances with high spatial and good energy resolution is necessary to understand their origin and properties. The best spatial, energy, and time resolution is achieved by electron beam spectroscopy [51, 52], which covers electron energy loss spectroscopy (EELS) [53, 54, 55], energy filtered transmission electron microscopy (EFTEM) [56], cathodoluminescence (CL) [57, 58], photoemission electron microscopy [59], photo-induced near-field electron microscopy [60], and electron energy gain spectroscopy [61]. However, electron beam spectroscopy in a transmission electron microscope requires placing the plasmonic antenna onto a very thin substrates like silicon nitride or silicon oxide membranes with the thickness below 50 nm. A very recent study introduces usage of a monolayer or a thin layer of hexagonal boron nitride [62].

Research in the field of plasmonics has a large tradition at the Insitute of Physical Engineering and CEITEC Brno University of Technology [63], mostly in the field of metasurfaces [64, 65], scanning near-field optical microscopy [66, 67, 68], quantitative phase imaging [64, 69], EELS [70, 71], fabrication [72, 73, 74, 75], and development of theory [76]. This work, focused on fabrication and characterization of plasmonics antennas by electron microscopy, freely follows previous investigations of plasmonic antennas by electron energy loss spectroscopy [70] and cathodoluminescence [77] and contributes to the publication of several manuscripts [71, 75, 78, 79, 80]. The main research results are divided into four parts.

Chapter 2 focuses on a comparative study of plasmonic antennas fabricated by electron beam and focused ion beam lithoghraphy [75]. The choice of preferred fabrication technique is rather important. My results show that the plasmonic response of the antennas characterized by EELS is considerably stronger and slightly better localized for the antennas fabricated by electron beam lithography than for the antennas fabricated by focused ion beam lithoghraphy. Therefore, while both techniques are suitable for the fabrication of plasmonic antennas, electron beam lithography shall be prioritized over focused ion beam lithography due to better quality of the resulting antennas.

Chapter 3 focuses on Babinet's principle of complementarity for gold disc-shaped plasmonic antennas. The emphasis is given on experimental study using spatially-resolved electron energy loss spectroscopy and cathodoluminescence to investigate electromagnetic response of elementary plasmonic antennas: gold discs and complementary disc-shaped apertures in a gold layer [71].

Chapter 4 discuses nanostructures with functional properties related to the local enhancement of electric and magnetic field. Such plasmonic antennas were studied theoretically using a combination of two types of electric-magnetic complementarity to increase the degree of freedom for the design of the antennas: bow-tie and diabolo duality and Babinet's principle [81]. Plasmonic modes in nanoparticle dimers with conductive (diabolo or inverted bow-tie antennas) or insulating (bow-tie or inverted diabolo antennas) junction were revisited in our study combining EELS, optical spectroscopy, and numerical simulations [80].

Chapter 5 deals with rather unique plasmonics on silver amalgam nanoparticles. It was experimentally proved that by changing the size of nanostructures the dipole LSP resonance can be tuned through the whole visible and infrared region. Therefore, nanostructured silver amalgam is proposed to be a prospective material for combination of electrochemistry and plasmonics [79].

2 Plasmonic antennas fabricated by electron beam and focused ion beam lithography

This Chapter summarizes a comparative study of plasmonic antennas fabricated by electron beam and focused ion beam lithography published in Scientific Reports [75]. Plasmonic antennas are often fabricated by electron beam lithography (EBL) or focused ion beam (FIB) milling. The EBL process consists of the following steps: (i) deposition of a resist sensitive to electron beam on a substrate, (ii) exposition of the resist to the electron beam and development of the resist (removal of exposed or unexposed regions of the resist), (iii) deposition of a thin layer of metal, and (iv) removal of the remaining resist covered by the redundant metal (lift-off) and final cleaning of the sample. FIB lithography is more straightforward, consisting of two steps: (i) deposition of a thin layer of metal and (ii) exposition to a focused ion beam that locally sputters off the metal (Figure 2.1). Both the EBL process and the FIB milling are capable to create sub-10-nm structures [35, 82].

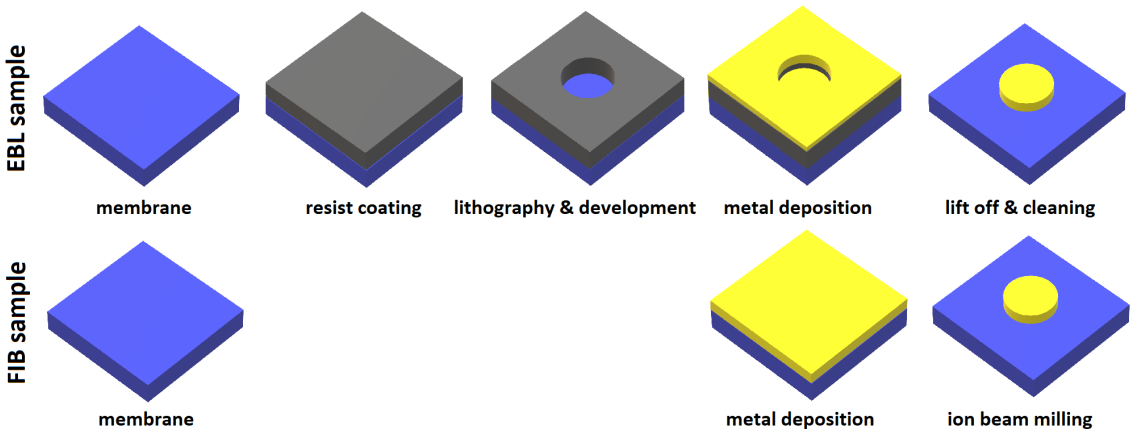

Figure 2.1: Schematic overview of individual steps in the fabrication process of the EBL and the FIB antennas.

Naturally, both fabrication techniques have their advantages and disadvantages. In EBL, final structures can be contaminated by the residual resist or solvents. Lift-off can exert a pronounced mechanical force that can damage the fabricated structure or even the substrate, which is particularly dangerous for thin membranes used as the substrate. In FIB, large-area mechanical effects are absent but the focused ion beam can damage the sample locally. Redeposition of sputtered-off metal atoms can reduce the quality of products of the technique. There are no chemicals involved in the process but the ions in

the milling beam and atoms sputtered from the metal and substrate can still contaminate the fabricated structures. EBL consists of more steps but is more suitable for large area lithography as the exposition, the only local process, is considerably faster than for FIB. On the other hand, FIB is faster when only a single antenna or a small field of antennas is being fabricated. For example, considering optimal parameters for FIB and EBL (see the Methods section), FIB milling of one antenna inside a $2 \times 2\,\mu m^2$ metal-free square takes typically 2 minutes. Array of 50×50 antennas is fabricated in 84 hours (3.5 days). On the other hand, in EBL the length of chemical processes (resist coating, development, and lift off) is independent on the number of fabricated antennas and takes typically 6 hours. Electron beam exposition of one antenna lasts far below 1 second; the array of 50×50 antennas is exposed in 5 seconds. FIB enables fabrication of single crystalline plasmonic antennas when a chemically grown single crystal gold flake transferred onto a substrate is used as the pristine material instead of a sputtered or an evaporated polycrystalline thin film [83, 84]. The quality of lithographically fabricated plasmonic antennas can be further enhanced by annealing which enlarges the grains and accordingly reduces the number of grain boundaries so the behavior of nanostructures is closer to a single crystal [43, 44]. It is clear that suitability of both methods depends on specific tasks and experimental comparison of the structures fabricated by both methods is of high importance for the judicious selection of the optimal method.

Four individual disc-shaped gold plasmonic antennas were studied in detail: two series prepared by both EBL and FIB consisting of antennas with designed diameters of 120 nm and 140 nm and with designed height of 25 nm. After their fabrication, several characterization methods have been applied. Some of those methods can modify the samples. In particular, a hydrocarbon contamination is developing during measurements in electron microscopes using high beam current (i.e., EELS and EDS) [85, 86]. For this reason, the characterization methods have been applied in specific order for all investigated antennas: EELS, EDS, AFM. As possible contamination is considered to be a part of PA functionality, no specific cleaning steps have been applied between individual measurements. In particular, no plasma cleaning has been applied prior to EELS measurements, although it is often used to remove the hydrocarbon contamination.

2.1 Methods

Standard 50 nm thick silicon nitride membranes for TEM with a window size of $250 \times 250\,\mu m^2$ and frame thickness of 200 µm by Silson Ltd. (UK) were used.

Electron beam lithography (EBL) was performed using the following procedure. As the resist, we used a 70 nm thick layer of poly(methyl methacrylate) 679.02 all-resist dissolved in ethyl acetate. The exposition has been performed within the Tescan MIRA3/RAITH SEM operated at 30 kV with the electron beam current of 100 pA and the dose of $320\,\mu C\,cm^{-2}$. Exposed samples were developed in the developer AR 600-56 all-resist for 3 minutes, as the stopper we used isopropyl alcohol for 30 seconds. Afterwards, the sample was cleaned by demineralized water for 30 seconds. Lift-off was performed by 4 hour acetone bath applying mega sound for 1 hour finished by acetone stream wash. Finally, the sample was cleaned by isopropyl alcohol for 30 seconds, followed by cleaning using ethanol for 30 seconds and demineralized water for 30 seconds. To prevent the collective interaction of the antennas we fabricated individual isolated antennas with a distance between two nearby antennas of 3 µm.

Metal deposition was done in the electron beam evaporator BESTEC. Pressure during

the deposition was in the order of 10^{-5} Pa and voltage was set to 8 kV. We deposited a 5 nm Ti adhesion layer at a deposition speed of $0.05\,\mathrm{nm\,s^{-1}}$ and a 25 nm Au layer at a deposition speed of $0.02\,\mathrm{nm\,s^{-1}}$. Metal pellets were purchased from Kurt J. Lesker Company. Membranes were rotated at a speed of 10 rpm (revolutions per minute) to ensure the homogeneity of the layers. Both samples were deposited during one session to have exactly the same metallic layer on both of them. During the deposition, the thickness of the layer was measured in situ by a quartz crystal microbalance monitor.

Focused ion beam (FIB) lithography was performed in the dual beam FIB/SEM microscope FEI Helios using gallium ions with the energy of 30 keV and ion beam current of 2.4 pA. The energy (the highest available) and the current (the lowest available) are optimized for the best spatial resolution of the milling. The antennas were located in the middle of a $2 \times 2\,\mu\mathrm{m}^2$ metal-free square, which is perfectly sufficient to prevent their interaction with the surrounding metallic frame [70].

Electron energy loss spectroscopy (EELS) measurements were performed with the TEM FEI Titan equipped with the GIF Quantum spectrometer operated in the monochromated scanning regime at 300 kV. The beam current was set to 0.8 nA and the FWHM of the ZLP was around 0.18 eV. The convergence angle was set to 10 mrad, the collection angle to 20.5 mrad, and the dispersion of the spectrometer to 0.01 eV/pixel. EELS spectrum images were recorded with the size of $300 \times 300\,\mathrm{nm}^2$ (100×100 pixels with the pixel size of 3 nm). Every pixel consists of 30 cross-correlated EEL spectra with the total pixel time of 20 ms. EEL spectra were integrated over the ring-shaped areas around the disc edge where the LSP resonance is significant (inner diameter about 50 nm, outer diameter about 200 nm) and divided by the integral intensity of the whole spectrum to transform measured counts to a quantity proportional to the loss probability. EEL maps were calculated by dividing the map of integrated intensity at the plasmon peak energy with an energy window of 0.1 eV by the map of the integral intensity of the zero-loss peak. Radial distributions of LSP resonances were calculated from the EEL maps by rotational averaging followed by the background subtraction (base level of the intensity in the EEL maps far away from the antennas).

Energy dispersive X-ray spectroscopy (EDS) measurement was performed on the TEM FEI Titan equipped with the Super-X spectrometer operated in the scanning regime at 300 kV. The electron beam current was set to 2 nA. EDS spectrum images were recorded with the size of $600 \times 600\,\mathrm{nm}^2$ (300×300 pixels with the pixel size of 2 nm) using integration of 100 images with the acquisition time of 10 µs per pixel. Spectrum images were post processed in the Velox software. EDS maps show the net intensity (i.e. background subtracted and artifact corrected intensity). EDS quantification in atomic percents was performed in the Velox software using a parabolic background model and Brown-Powell ionization cross-section model.

Atomic force microscopy (AFM) measurement was performed using the Scanning Probe Microscope Bruker Dimension Icon in the PeakForce Tapping mode, which enables larger control over applied force to prevent damaging the membrane [87]. The peak force setpoint was set to 5 nN, the scanning window was $400 \times 400\,\mathrm{nm}^2$ (256×256 pixels with the pixel size of 1.6 nm).

Numerical simulations of EELS spectra were performed using the MNPBEM toolbox [88, 89] based on the boundary element method (BEM). The dielectric function of evaporated gold was taken from Olmon et al. [90] and the dielectric function of the silicon nitride membrane was set to 4 [91]. The titanium adhesion layer has been neglected in the simulations. For the calculations of spectra the electron beam was positioned 2 nm from the outer side of the antenna. Obtained loss probability density was recalculated

to loss probability at 0.01 eV energy intervals (corresponding to the dispersion of the spectrometer in the experiment).

2.2 Results

The three-dimensional (3D) morphology of the antennas measured by EELS in terms of relative thickness is shown in Figure 2.2. The average relative thickness is (0.23 ± 0.05) for 120 nm EBL antenna, (0.20 ± 0.07) for 120 nm FIB antenna, (0.23 ± 0.05) for 140 nm EBL antenna, and (0.20 ± 0.06) for 140 nm FIB antenna, see also Figure 2.3d. The relative thickness is proportional to the absolute thickness of the antenna with the inelastic mean free path (IMFP) as the constant of proportionality. The IMFP in gold for the actual parameters of the electron beam (electron energy of 300 keV and collection semi-angle of 20.5 mrad) calculated using the software package EELSTools by D. Mitchell [92] applying the algorithm of K. Iakoubovskii et al. [93] equals to 113 nm. Consequently, the absolute thickness of the antennas is (23 ± 7) nm for FIB antennas and about (26 ± 6) nm for EBL antennas, which is in a good agreement with the desired value of 25 nm. Diameters of fabricated antennas measured from TEM micrographs indicate good agreement between the designed and actual value. They read (125 ± 5) nm for the 120 nm EBL antenna, (122 ± 6) nm for the 120 nm FIB antenna, (140 ± 6) nm for the 140 nm EBL antenna, and (142 ± 7) nm for the 140 nm FIB antenna.

There is a clear structural difference between EBL and FIB antennas. The EBL antennas have an irregular shape and their thickness varies rapidly with the position as the gold layer is polycrystalline with a grain size of about 20 nm. The FIB antennas are seemingly more uniform in the thickness and their edges are smooth and featureless. Nevertheless, a closer inspection (see Figure 2.3d) reveals even more pronounced thickness profile (i.e. with a larger amplitude) but smoother (i.e. with a reduced slope) variations of the thickness with a magnitude of nearly 10 nm. The flat boundary is mainly caused by two reasons. First, the metallic layer is deposited on the flat substrate for FIB but on the patterned resist for EBL forming a flat layer in the former case and frayed edges in the latter case. Second, the ion beam has a Gaussian-like profile which leads to smoothing of the edges. Additionally, the ion beam may result into amorphization and recrystallization of gold, smoothening its surface [94]. Finally, redeposition of sputtered-off gold may contribute to the smoothness of the gold surface and might be also partially responsible for the large magnitude of the thickness variation.

Next, EEL spectra were processed to obtain the loss probability related to LSP resonances. This included ZLP and background subtraction. The process is illustrated in Figure 2.3a showing the unprocessed low-loss part of the EEL spectrum decomposed into the contribution of ZLP and background, and signal corresponding to the LSP resonance for the 120 nm EBL antenna. Extracted EEL signal corresponding to the LSP resonance is shown in Figure 2.3b for 120 nm antennas and in Figure 2.3c for 140 nm antennas. Within the spectra a single broad peak corresponding to the dipole LSP mode is resolved. This assignment is further supported by the results of numeric simulations, also shown in Figure 2.3b,c. It is also in agreement with prior investigations of plasmonic disc-shaped antennas [95]. The second peak in the calculated spectra corresponds to the quadrupole LSP mode. Due to its low intensity and instrumental broadening, related to the energy width of the impinging electron beam with the FWHM of about 0.18 eV, this mode is not resolvable in the experimental data. The simulation predicts an energy of the dipole LSP mode of 1.66 eV for 120 nm antennas and 1.59 eV for 140 nm antennas. Measured

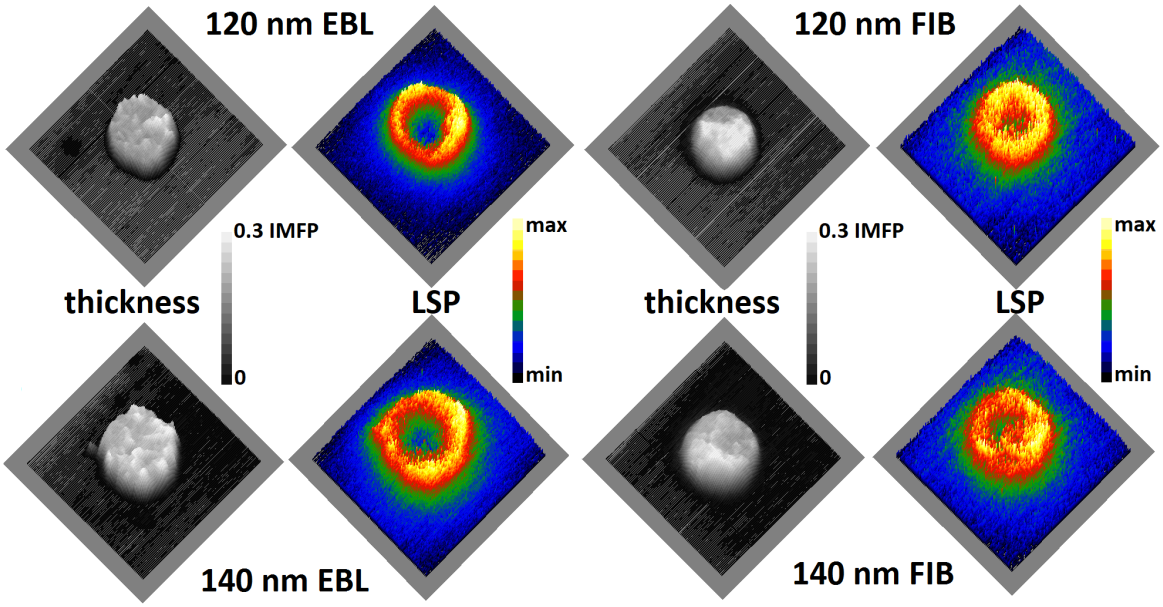

Figure 2.2: Thickness and LSP resonance mapping by EELS. 3D morphology of the antennas represented by the relative thickness (thickness in units of inelastic mean free path, IMFP) measured by EELS (left, grayscale) and EEL intensity maps showing the spatial distribution of LSP resonance at (1.60 ± 0.05) eV for 120 nm antennas and (1.40 ± 0.05) eV for 140 nm antennas (right, color scale). The size of all micrographs is $300 \times 300\,\mathrm{nm}^2$.

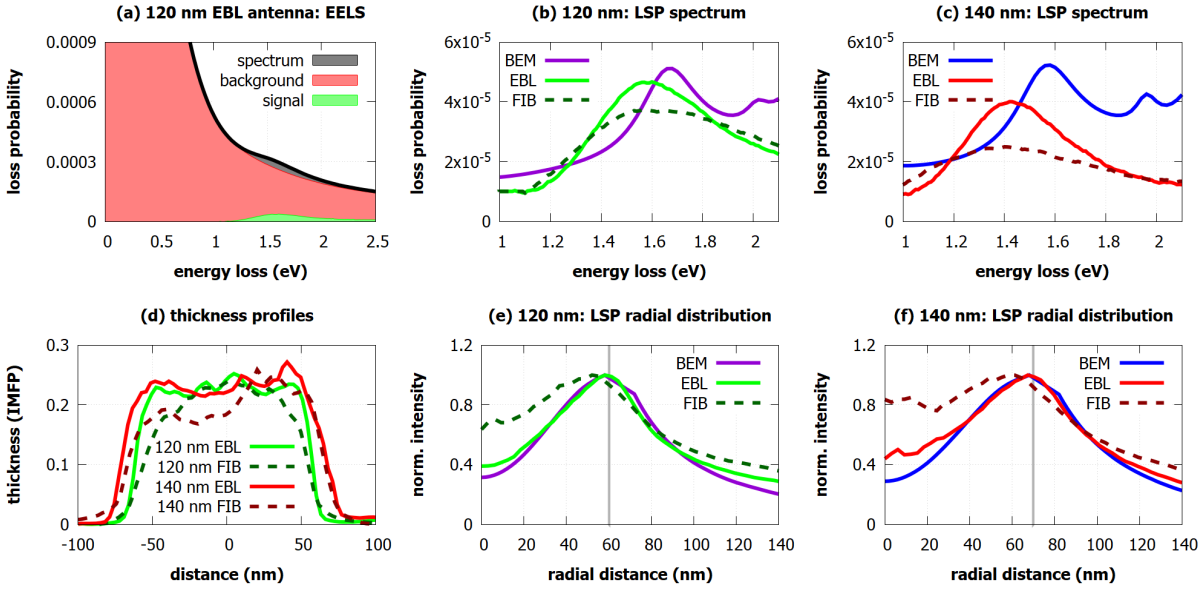

Figure 2.3: EELS measurement of LSP resonances. (a) Typical raw low-loss EEL spectrum (black) decomposed into background including zero-loss peak (red) and the signal corresponding to the LSP resonance (green) for the 120 nm EBL antenna. (b,c) Loss probability related to LSP measured by EELS in the EBL and the FIB antennas together with the calculated values obtained by BEM for 120 nm (b) and 140 nm (c) antennas. (d) Thickness profiles (thickness in units of inelastic mean free path, IMFP) of the antennas determined by EELS. We note that EBL antennas have slightly sharper edges. (e,f) The radial distribution of the LSP-related loss probability (at the energy of its maximum) for 120 nm (e) and 140 nm (f) antennas measured by EELS for EBL and FIB antennas and calculated by BEM. Antennas have their center at 0 nm and the edge of antennas is marked by the grey line.

LSP resonance energy is (1.56 ± 0.09) eV for 120 nm EBL antenna, (1.62 ± 0.09) eV for 120 nm FIB antenna, (1.43 ± 0.09) eV for 140 nm EBL antenna, and (1.41 ± 0.09) eV for 140 nm FIB antenna. The measured energies are thus systematically red-shifted from the calculated energies, although the magnitude of the shift is rather minor and ranges between 0.04 eV and 0.18 eV. Such a red-shift can be attributed to the deviations of the actual antenna shape from the ideal disc, inhomogeneous thickness of antennas, modification of the dielectric function of gold due to grain boundaries and polycrystallinity of the antennas [45, 46], or effects induced by the contamination [96] and Ti adhesion layer [41, 42].

If we compare EBL and FIB antennas, we observe more intense peak for EBL antennas. Figure 2.2 shows the spatial distribution of the LSP resonance in the form of intensity maps at the energy of (1.60 ± 0.05) eV for 120 nm antennas and (1.40 ± 0.05) eV for 140 nm antennas. The radial dependences of the intensities averaged over the polar coordinate are shown in Figure 2.3e,f. The maximal intensity of LSP resonance is confined to sharp features on the edges of EBL antennas. In the case of FIB antennas, LSP resonance is less confined to the edges of the structures and the EEL intensity maps are blurred, which can be caused, for example, by thickness fluctuation or contamination.

Following the EELS measurements the chemical composition of the antennas including their possible contamination was analyzed by EDS, which enables detection of all elements heavier than Be in one measurement. We have detected and further focused on the following chemical elements: Si and N constituting the membrane, Au and Ti constituting the antenna and the adhesion layer, respectively, Ga that forms the ion beam in FIB and can be implanted into the sample, C and O as frequent contaminants. Spatial distribution of the intensity of characteristic X-ray radiation for these elements is shown in Figure 2.4 for both FIB and EBL antennas with the diameter of 140 nm together with the bright field TEM and high-angle annular dark field (HAADF) STEM micrographs. We distinguish in total three areas with different chemical composition, denoted as Area 1 to 3 in the following. Area 1 corresponds to the antenna and Areas 2 and 3 to its surrounding exposed and unexposed to the electron beam during EELS measurements, respectively. We note that the composition of Areas 2 and 3 is almost identical with the exception of carbon, which has a stronger presence in the Area 2 (exposed to the electron beam) in the case of FIB antenna (see the intense red square in Figure 2.4). The distribution of individual elements within each Area is homogeneous. The average relative atomic rate of each element for each Area is given in Table 2.1. As the thickness of different Areas is not identical, we note that the atomic rates between different Areas are not directly comparable but have to be rescaled to the same thickness.

Both Si and N exhibit almost identical X-ray intensity over all Areas for both FIB and EBL antennas. Slightly increased intensity of Si below the antennas (Area 1) is an artifact related to the secondary emission of X-rays in the silicon-based EDS detector associated with larger thickness and density of this Area. Average stoichiometry of the silicon nitride membrane (neglecting Area 1) reads $Si_3N_{2.0\pm0.6}$. Verification measurement by EELS resulted into average stoichiometry $Si_3N_{1.8\pm0.3}$ which is in a very good agreement with EDS. Gold is present only at the antennas (Area 1), underpinning reliability of both fabrication techniques. In general, EDS is not accurate enough to assess the thickness of the gold layer. It is nevertheless illustrative to provide a rough estimate. The atomic rate of Au is 0.18 ± 0.03 and 0.16 ± 0.03 in the EBL and FIB antenna, respectively. These values are equal within the experimental error. The atomic rates of Si and N are listed in Table 1. We now rescale the atomic rates to the volume rates using covalent radii of N, Si, and Au reading 71 pm, 116 pm, and 124 pm [97]. Considering the thickness of the

Table 2.1: Chemical composition of the membranes with EBL and FIB antenna in atomic percents determined by EDS after the EELS measurement. The composition is averaged over one of three areas with homogeneous chemical compositions: Area 1 corresponds to the antenna, while Areas 2 and 3 corresponds to their surrounding exposed and unexposed to the electron beam during EELS measurements, respectively.

	EBL antenna			FIB antenna		
	Area 1	Area 2	Area 3	Area 1	Area 2	Area 3
Au	$(18 \pm 3)\,\%$	$< 1\,\%$	$< 1\,\%$	$(16 \pm 3)\,\%$	$< 1\,\%$	$< 1\,\%$
Ti	$(4 \pm 1)\,\%$	$< 1\,\%$	$< 1\,\%$	$(4 \pm 1)\,\%$	$(2 \pm 1)\,\%$	$(2 \pm 1)\,\%$
Si	$(35 \pm 5)\,\%$	$(55 \pm 5)\,\%$	$(55 \pm 5)\,\%$	$(32 \pm 5)\,\%$	$(40 \pm 5)\,\%$	$(45 \pm 5)\,\%$
N	$(20 \pm 3)\,\%$	$(35 \pm 5)\,\%$	$(35 \pm 5)\,\%$	$(17 \pm 3)\,\%$	$(25 \pm 5)\,\%$	$(33 \pm 5)\,\%$
C	$(13 \pm 3)\,\%$	$(4 \pm 2)\,\%$	$(4 \pm 2)\,\%$	$(25 \pm 5)\,\%$	$(25 \pm 5)\,\%$	$(8 \pm 3)\,\%$
O	$(6 \pm 2)\,\%$	$(4 \pm 2)\,\%$	$(4 \pm 2)\,\%$	$(5 \pm 2)\,\%$	$(7 \pm 2)\,\%$	$(7 \pm 2)\,\%$
Ga	$< 1\,\%$	$< 1\,\%$	$< 1\,\%$	$< 1\,\%$	$(3 \pm 1\,\%$	$(3 \pm 1)\,\%$

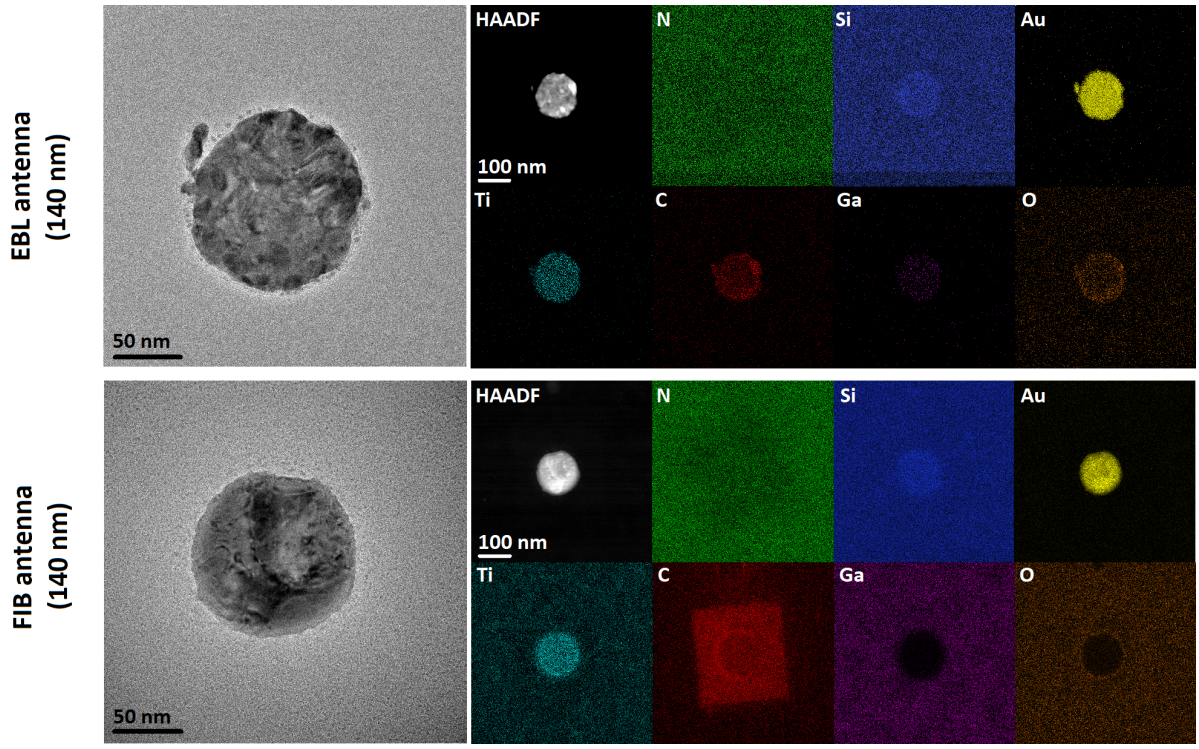

Figure 2.4: TEM micrographs and elemental maps showing chemical composition of 140 nm antennas. Left: TEM bright field micrographs of 140 nm EBL and FIB antennas. Right: STEM-HAADF image of the antennas presenting the distribution of heavy elements and spatial maps of element-specific X-ray intensity obtained from EDS for N, Si, Au, Ti, C, Ga, and O.

silicon nitride membrane of 50 nm, we obtain rough estimates of the thickness of the gold layer equal to 28 nm and 27 nm for the EBL and FIB antenna, respectively, in a good agreement with the designed thickness of 25 nm and EELS measurements of 23 nm to 26 nm.

Ti is present in the Area 1 for the EBL antenna but in all Areas for the FIB antenna. Apparently, FIB lithography was unable to fully remove Ti from the desired Areas as the sputter rate of Ti is much smaller than that of Au. Estimated thickness of the Ti contamination layer is 1 nm to 2 nm. Ga ions have been implanted to Areas 2 and 3 (i.e. into the antenna surrounding) for the FIB antenna. The atomic rate of Ga reads 0.03 ± 0.01. Importantly, no Ga contamination is found directly above or inside antennas (i.e. in Area 1), suggesting its rather limited influence on the plasmonic response of the antennas.

Finally, C and O are present as usual contaminants due to several reasons. The EBL antenna indicates larger contamination in Area 1 (i.e., at the position of the antenna) where the atomic rate of C reads 0.13 ± 0.03 and the atomic rate of O is 0.06 ± 0.02. This is probably the result of incomplete resist removal during the development of lithographic pattern. The antenna surrounding (Areas 2 and 3) indicates low level of C and O contamination with the atomic rate of both elements of 0.04 ± 0.02. Such low levels of contamination refers to usual contamination of the sample when it is exposed to air. The FIB antenna indicates much higher C and O contamination. The sample has been contaminated by organic residues present in the FIB chamber. C is particularly strongly present in the areas exposed to the electron beam during the EELS measurement [85, 86] (Areas 1 and 2 corresponding to the intense red square in Figure 2.4) and its atomic rate reads 0.25 ± 0.05. Area 3 then exhibits the atomic rate of C of 0.08 ± 0.03 which is a higher value than for the EBL antenna. The atomic rate of O reads 0.05 ± 0.02 in Area 1 and 0.07 ± 0.02 in Areas 2 and 3 (i.e., in the antenna surroundings) which may indicate that Ti and Ga contaminants present in the surroundings are partially oxidized.

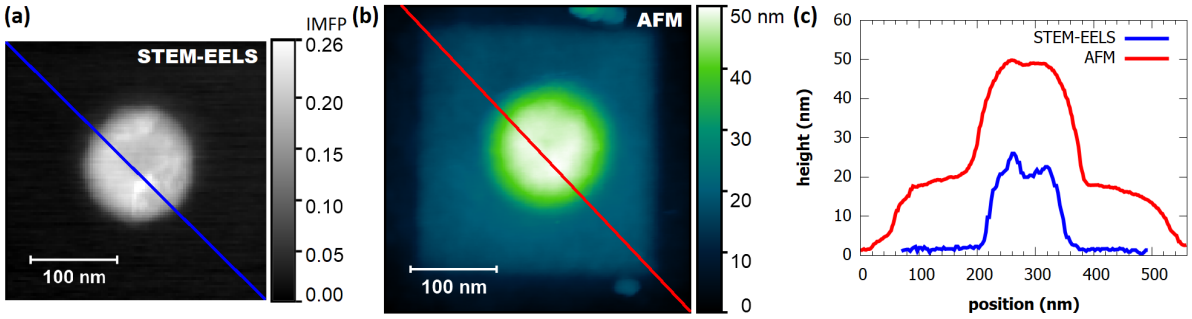

Figure 2.5: Thickness profile of a 140 nm FIB antenna and the hydrocarbon contamination on its surface. (a) Relative thickness (thickness in terms of IMFP) of the antenna retrieved by EELS. (b) Topography of the antenna including the hydrocarbon contamination measured by AFM. (c) Cross-sections of thickness profiles along the lines shown in (a) and (b). Relative thickness is recalculated to absolute thickness using the IMFP in gold of 113 nm. Blue line shows the thickness profile of the antenna determined by EELS, red line shows the thickness profile of the antenna and the contamination layer determined by AFM.

It is impossible to determine the thickness of hydrocarbon contamination layer on the FIB antennas using EELS because the contamination would further evolve during the measurement. Therefore, we have characterized surface topography of antennas by AFM measurement. Figure 2.5 compares the thickness of the 140 nm FIB antenna measured by EELS (assuming low hydrocarbon contamination) and surface topography measured

by AFM after the EELS measurements (with hydrocarbon contamination being fully developed). The thickness of the hydrocarbon contamination layer is uniform over the whole area of EELS measurement (Areas 1 and 2) with an average thickness of (18 ± 5) nm determined as the height difference between Areas 2 and 3.

2.3 Conclusion

The choice of a preferred fabrication technique should also consider the time and potential risks of the fabrication process. FIB preparation is simple and more straightforward as no chemistry is used and fast for individual antennas or small series of antennas. Moreover, FIB lithography exerts low mechanical strain and thus enables processing of pristine materials with low adhesion to the substrate such as chemically grown single-crystalline gold flakes. EBL preparation provides generally antennas of a higher quality, but the lithographic process induces potential risks of damaging the sample as the wet chemistry is used. EBL is more time consuming than FIB if a small number of antennas is prepared, but much faster if a large array of antennas is fabricated. In such case, the volume of material to be removed by FIB is too large. Therefore, either of the techniques is suitable for a different class of targeted nanostructures. In general, when no specific issues apply, EBL shall be prioritized over FIB as it produces antennas with stronger plasmonic response and low contamination.

In conclusion, we have performed the comparative study of plasmonic antennas fabricated by EBL and FIB. We have demonstrated that the EBL antennas have better quality. First, they have rather homogeneous thickness profile with decent thickness fluctuation, and sharper edges. Second, they are cleaner, with a moderate contamination of organic origin evidenced by the presence of carbon and oxygen atoms with the total rate up to 20 %. On the other hand, plasmonic antennas fabricated by FIB lithography have slightly dull edges and exhibit pronounced thickness fluctuation. They are also strongly contaminated not only by organic contaminants forming a continuous layer of the thickness of about 18 nm, but also by residues of FIB milling including implanted milling ions and atoms of the titanium adhesion layer, possibly oxidized. In consequence, the plasmonic response of the antennas characterized by EELS is considerably stronger and slightly better localized for the antennas fabricated by EBL than for the antennas fabricated by FIB. To conclude, while both techniques are suitable for the fabrication of plasmonic antennas, EBL shall be prioritized over FIB lithography due to better quality of the resulting antennas.

3 Babinet's principle for disc-shaped plasmonic antennas

Babinet's principle relates the optical response of apertures in thin films and their complementary analogues – solid barriers or particles. Originating in the wave theory of light and analysis of diffraction, it has recently entered the field of plasmonics [28]. According to the Babinet's principle assuming the metallic layer as infinitesimally thin ideal conductor, localized surface plasmons in complementary particles and apertures have identical resonance energies and their near fields are closely linked: The electric field distribution with a specific in-plane polarization for an aperture corresponds to the magnetic field distribution with a perpendicular polarization for a particle [98]. However, the real metallic layer is not an ideal and infinitesimally thin conductor, therefore a perfect complementarity is not fully expected and some differences may arise from the imperfect complementarity. Moreover, some additional differences can be related to fabrication processes and experimental techniques involved in the characterization of the real structures.

3.1 Methods

To assess the theoretically predicted Babinet's complementarity, a set of gold disc-shaped antennas and complementary apertures in a gold layer, schematically shown in Figure 3.1, with various diameters were studied. Plasmonic structures were fabricated by FIB lithography of the 30 nm thick gold layer on the 3 nm thick titanium adhesion layer on a silicon nitride membrane. EEL and CL spectra have been measured for several disc-shaped plasmonic particles and apertures with diameters between 43 nm and 164 nm.

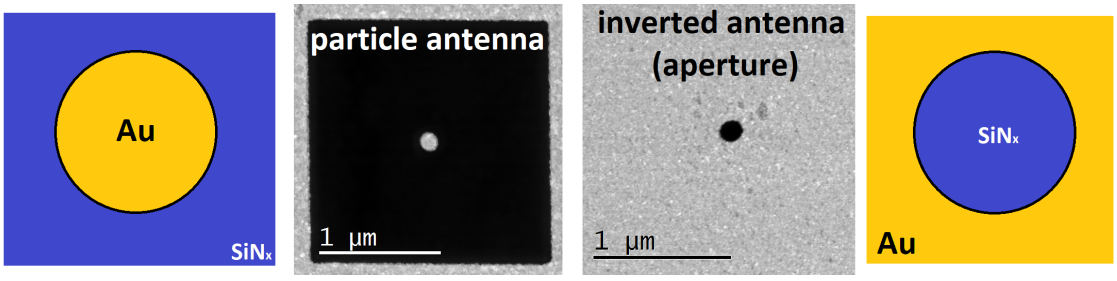

Figure 3.1: Schematic representation and dark field micrograph of a gold disc antenna and an aperture in the gold layer fabricated by FIB lithography.

Raw EEL spectra were processed by ZLP and background subtraction and normalized by dividing the spectra by the integral intensity of the ZLP with the interval of integration from −1 eV to 1 eV. A typical LSP related loss probability spectrum (for a disc with the diameter of 101 nm) is shown in Figure 3.2. The theory predicts two distinct LSP modes

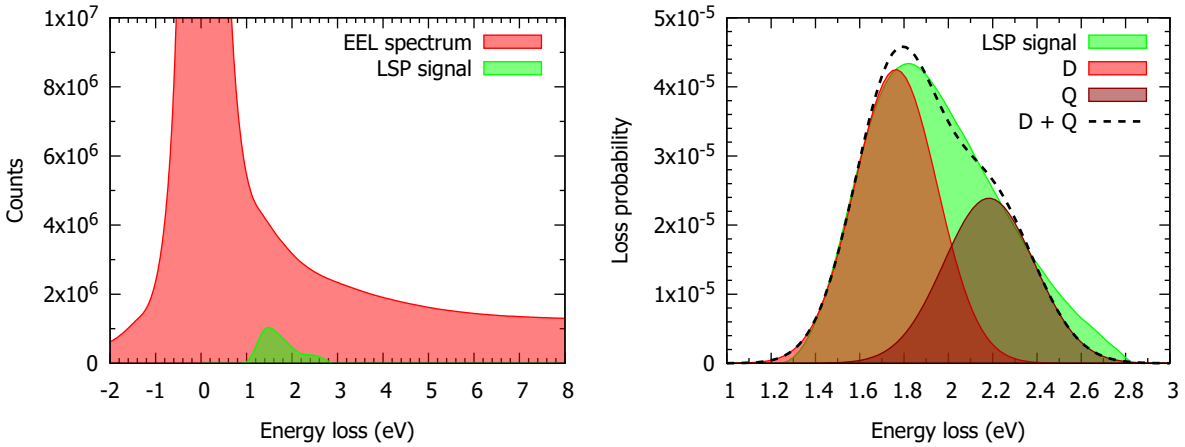

Figure 3.2: Processing of experimental EEL spectra. First, the EEL spectrum recorded for a disc with the diameter of 101 nm is decomposed into a zero-loss peak and background (red area), and LSP related response (green area). Second, the normalized LSP related EEL spectrum (green area) is decomposed into individual Gaussian peaks corresponding to the dipole mode (D) and the second peak corresponding to the quadrupole mode (Q) which is also influenced by the multimodal assembly.

(dipole and quadrupole), but the experimental EEL spectrum features only a single broad peak due to finite experimental resolution mostly limited by the energy distribution of the incident electron beam. Therefore, the experimental spectrum is further decomposed into individual peaks by sequential fitting of two Gaussians. The left side of the peak is fitted by a single Gaussian and the residual spectrum is processed in the same way. In this way, two peaks arising from the excitation of two distinct LSP modes or their superposition can be obtained. The first (lower energy) peak always represents the dipole LSP resonance. The second peak, however, cannot be always related with the quadrupole LSP resonance as it is contributed also by higher-order modes and corresponds thus to a mixture of the quadrupole mode with a multimodal assembly. Further, it is contributed by the bulk absorption that becomes important above 2 eV.

The loss probability maps were obtained by integration the total loss probability (including the ZLP and background) over the 0.1 eV wide energy window centered around the peak energy of the dipole mode and dividing this by the integral of total loss probability across the ZLP using an energy window from -1 eV to 1 eV. Such normalization is important to compensate the intensity differences caused by the different thickness of the parts of the sample covered and uncovered by gold.

3.2 Results

Experimental EEL and CL spectra of disc-shaped plasmonic antennas of different diameters excited near their edge are shown in Figure 3.3 and Figure 3.4, respectively. Within the EEL spectra it is possible to identify two peaks corresponding to the dipole LSP mode and the quadrupole mode mixed together with the multimodal assembly. In the CL spectra, just the dipole LSP mode is present as it is optically active, the higher modes have no net electric dipole moment and are thus optically dark. The peak energies of the detected LSP modes are displayed as functions of an effective wave number in a form of dispersion relations. The effective wave number is in the case of the dipole mode equal to the reciprocal antenna diameter, determined from ADF-STEM images. In the case of the

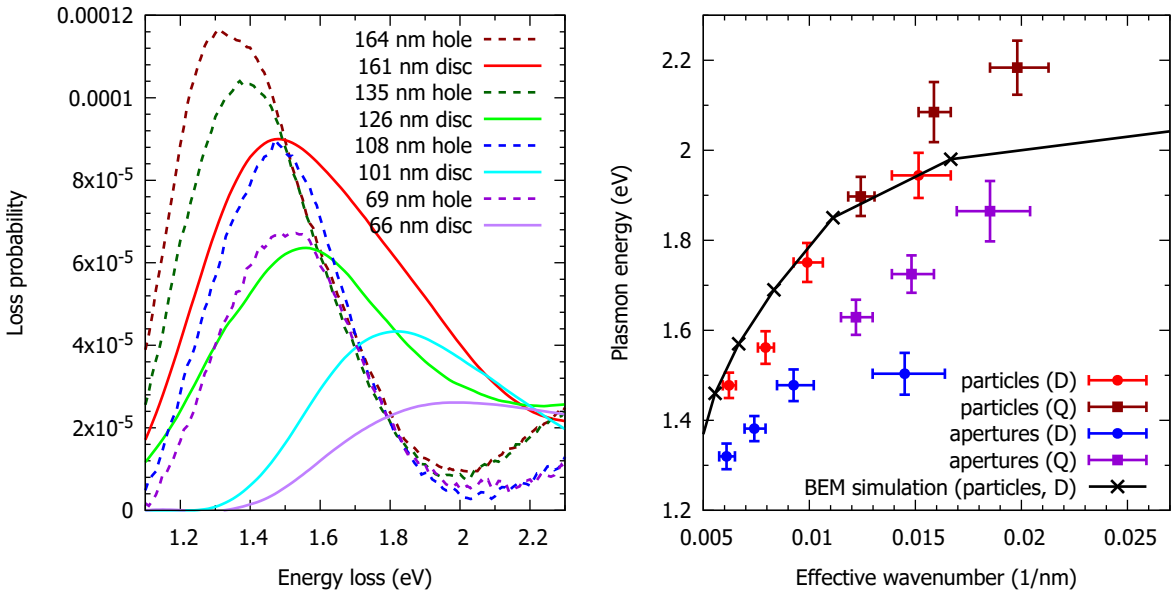

Figure 3.3: Measured EEL spectra of LSP resonance in gold nanodiscs and complementary apertures of different diameters (left) and the dispersion relation of measured LSP resonances by EELS (right). The peak energy is plotted as a function of the effective wavenumber, which corresponds to the reciprocal diameter in the case of the dipole mode or to the reciprocal value of the doubled diameter in the case of the quadrupole mode. To allow a brief comparison with the theory, BEM simulation of the dipole mode in gold nanodiscs is included.

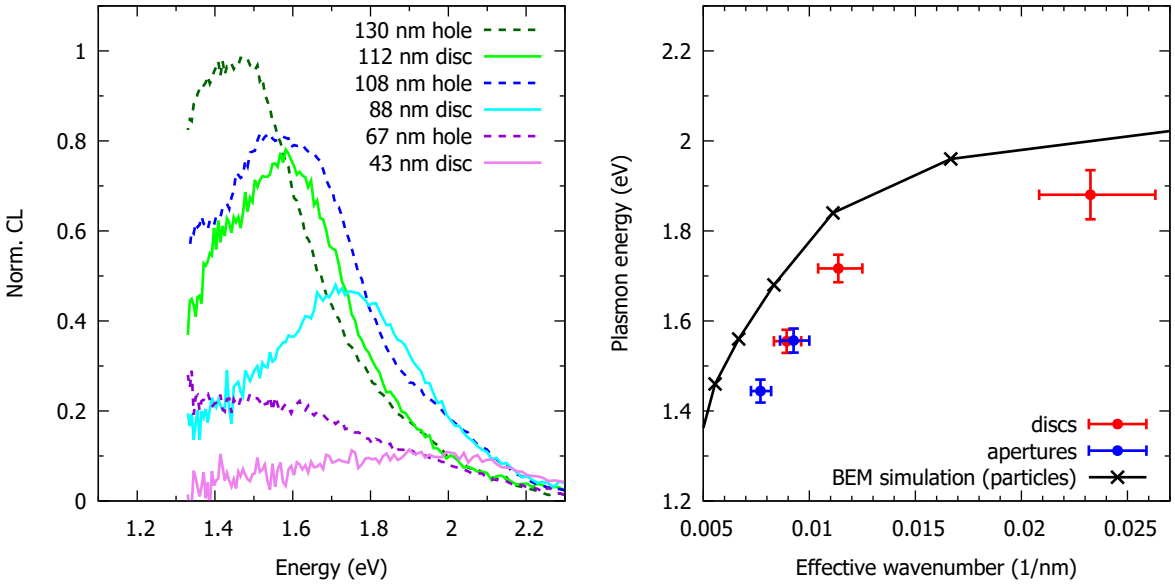

Figure 3.4: Measured CL spectra of LSP resonance in gold nanodiscs and complementary apertures of different diameters (left) and the dispersion relation of measured LSP resonances by CL (right). The peak energy is plotted as a function of the effective wavenumber, which corresponds to the reciprocal diameter. To allow a brief comparison with the theory, BEM simulation of the dipole mode in gold nanodiscs is included.

quadrupole mode, the effective wave number equals to the reciprocal value of the doubled antenna diameter. The error bars correspond to circles inscribed and circumscribed to the STEM micrographs of the antennas. The error bars of the energies include a standard error of the fit and a systematic error primarily related to the background subtraction and in the case of EELS to FWHM of the ZLP. To verify the measured results, a set of BEM simulations was computed. In simulations, the titanium adhesion layer was neglected, the dielectric function of gold was taken from Reference [99], and the dielectric constant of the silicon nitride membrane was set equal to 4 (in agreement with Reference [91]). The energy of the LSP dipole resonance in discs was calculated and is plotted in Figures 3.3 and 3.4 as the reference. Electron energy loss probability, the reference for EELS, and the radiative probability, the reference for CL, were evaluated separately. The energy of the dipole LSP resonance from simulations corresponds quite well to the measured value.

The energies of the dipole LSP mode determined by EELS and CL correspond to each other within the error bars. The agreement in the plasmon energy of disc and holes is excellent in the case of CL measurement. However in the case of EELS, a systematic redshift of apertures is observed. The only exception is the smallest aperture for which CL features no clear peak and the peak energy determined by EELS is strongly redshifted. The origin of this difference is at present not fully clear. Babinet's complementarity was therefore confirmed for the main LSP properties such as the resonance energies, but differences were found, for example, for the excitation efficiency as the measured response of the apertures is higher than for particles. This difference can be attributed to more efficient coupling of the apertures to the electromagnetic field of the relativistic electron or to the quality of fabricated antennas.

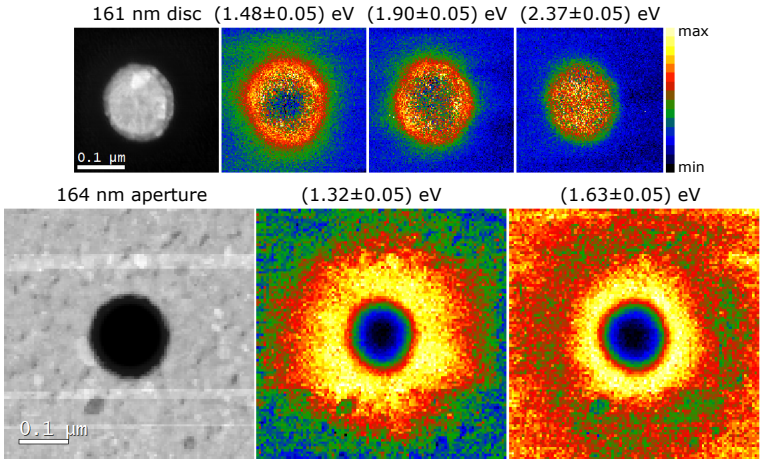

Figure 3.5: Dark field micrograph of gold disc antenna and aperture with the diameter of 161 nm and 164 nm, respectively, followed by loss probability maps showing the spatial distribution of the modes: the dipole (1.48 eV disc, 1.32 eV aperture), the quadrupole (1.90 eV disc, 1.63 eV aperture), and in the case of the disc also the breathing mode (2.37 eV).

Figure 3.5 shows the spatial distribution of all LSP modes detected by EELS in the largest antennas. To allow for a quantitative comparison of rather noisy data and taking into account the radial symmetry, the intensity profile in the loss probability maps in Figure 3.5 was averaged over the angular coordinate. The radial dependencies are displayed in Figure 3.6. For both the dipole and the quadrupole mode the loss probability is the strongest nearby the edge of the antennas, peaking at the inner side of the boundary in the particle and at the outer side of the boundary in the aperture, it means, inside the metal near the edge of the structure. As it is expected, the quadrupole modes are more spatially

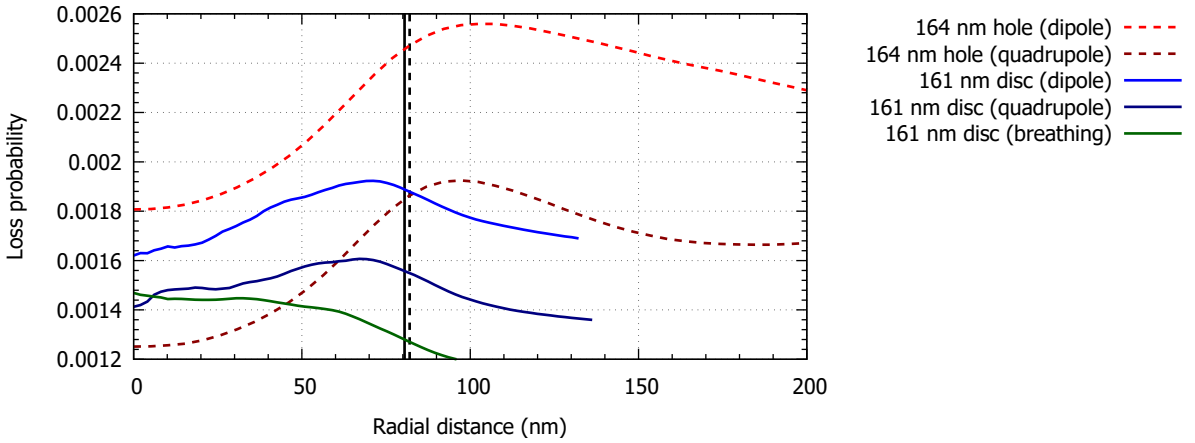

Figure 3.6: Radial dependence of the loss probability at the energy corresponding to the dipole, quadrupole, and breathing mode in the antenna and aperture with the diameter of 161 nm and 164 nm, respectively, obtained by rotational averaging of the intensity profile in loss probability maps in Figure 3.5. The black solid line denotes the radius of the disc and the black dashed line denotes the radius of the aperture, respectively.

confined than the dipole modes. The breathing mode in the disc has its maxima in the middle of the disc and its intensity decreases with the increasing distance. The important result is that the modes in apertures are considerably more extended and stronger (the loss probability is higher) than the modes in particles. This can be contributed by two effects. First, electric near field of the modes is less extended (exhibits faster asymptotic decay) than the magnetic near field in the particles, while the opposite holds (in line with Babinet's principle) in the apertures. In line with this finding the possibility to employ Babinet's principle for the imaging of the near magnetic field is revisited. It has been proposed that difficult-to-access magnetic near field can be represented by the electric near field in the complementary structures [100, 101]. While this approach was proven successful in THz [100], our results indicate its rather limited applicability for the near infrared and visible spectral range and for using EELS as the magnetic imaging technique.

3.3 Conclusion

In conclusion, solid and hollow disc-shaped plasmonic antennas exhibit Babinet's complementarity. Both types of plasmonic antennas exhibit LSP resonances of the comparable energy and the related near fields have complementary spatial distribution. On the other hand, we have found quantitative differences. Most prominent differences have been found for the near fields represented by the spatial distribution of loss probability as the plasmonic response of apertures is generally stronger and less confined to the edge of the structure. From the practical point, the observed differences are rather minor. The validity of the Babinet's principle is relevant also for numerous applications. Babinet's complementarity allows to toggle between the magnetic and electric response, or between the reflection and transmission mode. While particles have to be supported by a substrate, substrate-less apertures self-supported by their frame can be fabricated. Apertures also offer better heat and charge management as the thin metallic film surrounding the apertures is usually better conductor than the substrate supporting the particles. This opens the possibility of choice between both types of plasmonic antennas depending on desired fabrication limitations and operational conditions in a wide field of applications.

4 Plasmonic antennas with electric and magnetic hot spots

This Chapter summarizes a study of nanostructures with electric and magnetic hot spots – areas of strong local enhancement of electric and magnetic field. Such effects are supported by bow-tie [103] and diabolo [104] antennas. Four types of plasmonic antennas are introduced applying bow-tie and diabolo duality together with the Babinet's principle [81]: bow-tie and diabolo antenna as plasmonic antennas in the form of particles, and inverted bow-tie and inverted diabolo antenna as plasmonic antennas in the form of apertures. These four types of plasmonic antennas are schematically shown in Figure 4.1. Plasmonic modes in nanoparticle dimers with conductive (diabolo or inverted bow-tie antennas) or insulating (bow-tie or inverted diabolo antennas) junction has been characterized in our study combining EELS, optical spectroscopy, and numerical simulations [80].

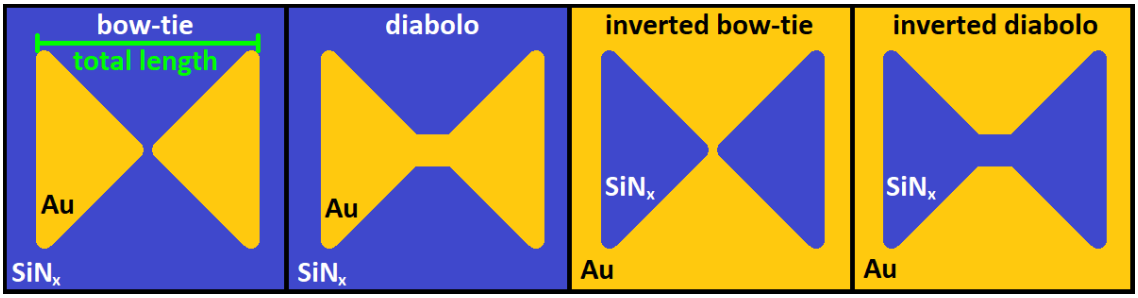

Figure 4.1: Schematic representation of bow-tie, diabolo, inverted bow-tie, and inverted diabolo antenna. The green bar denotes the total length of the antenna which is used as the characteristic parameter for all antennas.

4.1 Methods

Gold plasmonic antennas were fabricated on a 30 nm thick silicon nitride membrane by focused ion beam lithography of deposited 30 nm thick polycrystalline gold layer. It should be noticed that no adhesion layer was used. Direct antennas were situated in the middle of a metal-free square between 1 µm × 1 µm and 4 µm × 4 µm, which is perfectly sufficient to prevent their interaction with the surrounding metallic frame. Inverted antennas were fabricated as isolated antennas with the distance between two nearby structures of at least 5 µm to prevent their collective interaction. Figure 4.1 shows the design of the bow-tie, diabolo, inverted bow-tie, and inverted diabolo plasmonic antennas. Particle antennas consist of two metallic wings and a bridge which is insulating for a bow-tie and metallic for a diabolo. For inverted structures, metallic and insulating parts are interchanged. The dimensions of the bridge are set to approximately 30 nm × 30 nm and the total length of

the plasmonic antenna is varied. The wing angle is set to 90° which ensures the maximal complementarity of direct and inverted antennas as the area with gold and without gold is in the square with the edge corresponding to the total length of the antenna is nearly the same. Bow-tie and inverted diabolo antennas concentrate charge and form electric hot spots while diabolo and inverted bow-tie antennas funnel current and form magnetic hot spots [81].

Plasmon resonances were characterized using EELS and partially CL. EELS measurements were performed with TEM FEI Titan equipped with GIF Quantum spectrometer operated in monochromated scanning regime at 300 kV. Beam current was set to 0.4 nA and the FWHM of the ZLP was around 0.1 eV. Convergence angle was set to 10 mrad, collection angle to 10.4 mrad, and dispersion of the spectrometer to 0.01 eV/pixel. EELS spectrum images were recorded with the pixel size of 5 nm (except the largest structures where the pixel size was increased), while the number of pixels depended on the antenna size. Every pixel consists of 30 cross-correlated EEL spectra with the total pixel acquisition time around 25 ms. EEL spectra were integrated over several pixels around the positions of interest, background and zero-loss peak subtracted, and divided by the integral intensity of the whole spectrum to transform measured counts to a quantity proportional to the loss probability. EEL maps were obtained as energy-integrated intensity at the plasmon peak energy with the energy window of 0.1 eV divided by the integral intensity of the ZLP with the integration window from -0.5 eV to 0.5 eV. Such normalization is important to compensate the intensity differences caused by the different thickness of the parts of the sample covered and not-covered by gold. CL measurement was performed on the TEM FEI Tecnai F20 with the Gatan VULCAN spectrometer operated in scanning regime at 200 kV. Beam current was set to 13 nA, the central wavelength was set to 800 nm which corresponds to detectable energy range from 1.24 eV to 2.25 eV, the acquisition time was set to 2 s/pixel, and the CL signal was collected from both mirrors (upper and lower) together.

4.2 Bow-tie and inverted bow-tie antennas

A typical bow-tie antenna with the total length of 282 nm and a typical inverted bow-tie antenna with the total length of 300 nm are shown in Figure 4.2. The EEL spectra recorded at different positions reveal three distinct peaks. The nature of modes corresponding to these three peaks is revealed in the loss probability maps at peak energies shown in Figure 4.3.

The first peak in Figure 4.2 is detected at 1.23 eV in the case of bow-tie and at 1.08 eV in the case of inverted bow-tie, respectively. The spatial distribution of the loss probability at the energy of the first peak exhibits maxima in the corners of the bow-tie and therefore corresponds to a transverse dipole mode as it is oriented perpendicular to the total length of the structure. The transverse dipole mode is the lowest mode of this structure as the wing angle is set to 90° which implies the longest length of the metal piece of the bow-tie antenna in the transverse direction. It is a mixture of a bonding and an antiboding mode consisting of parallel and antiparallel alignment of the dipoles in both wings (Figure 4.3 shows the antibonding case). Their energy difference is in this case so low that they are not distinguishable by EELS. In the case of the inverted bow-tie, the energy of this mode is similar. However, the spatial distribution is rather different. From the Gauss law it follows that the strongest out-of-plane electric field, detected by EELS, occurs just near the areas of an accumulated charge. Therefore, in the case of the particle

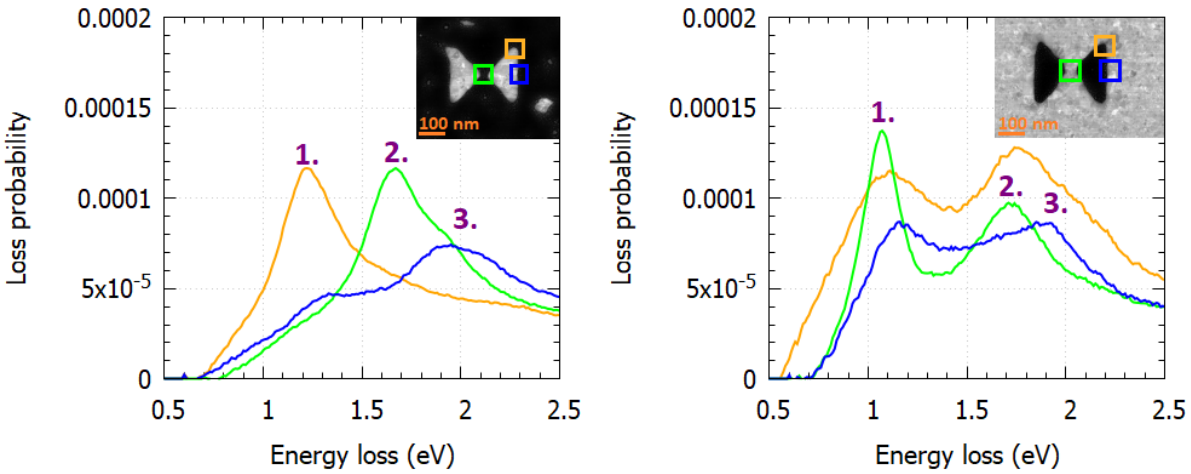

Figure 4.2: Background and ZLP subtracted normalized EEL spectra measured in the corner (orange), in the gap (green), and on the outer edge (blue) of the bow-tie (left) and the inverted bow-tie (right) antenna. The color squares in the insets indicate the areas where the respective spectra were collected. The first peak corresponds to the transverse dipole mode, the second one to the longitudinal dipole mode, and the third one to the edge mode. For better description of these modes, see Figure 4.3.

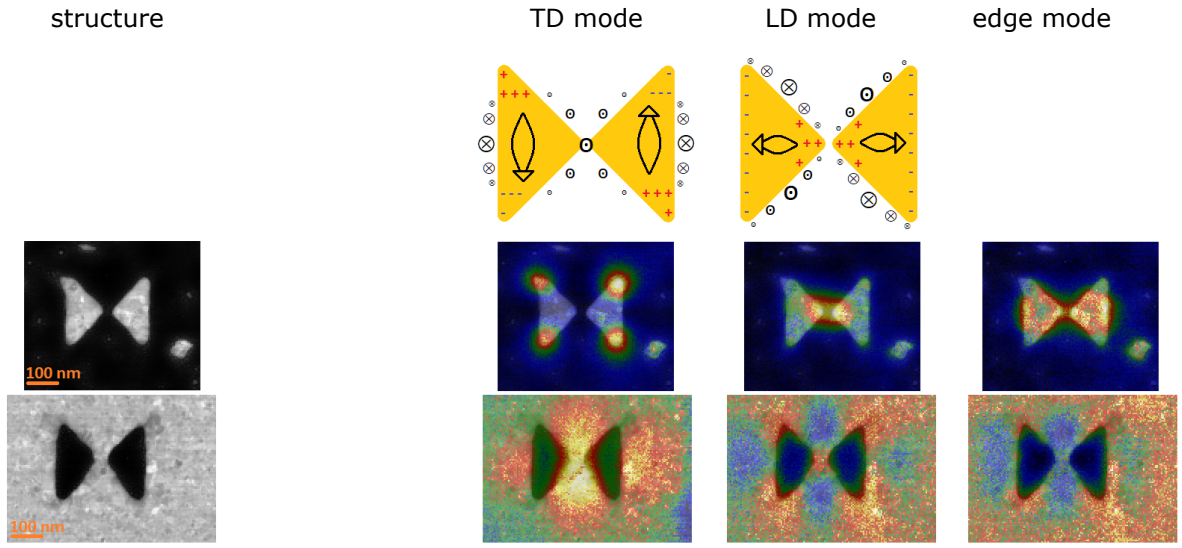

Figure 4.3: Schematic representation of detected plasmonic modes in the bow-tie antenna followed by experimental data corresponding to the transverse dipole (TD) mode, the longitudinal dipole (LD) mode, and the edge mode represented by loss probability maps at peak energies determined from Figure 4.2 placed over a shadow of the micrograph of the antenna shown in the left column. From the Gauss law it follows that the strongest out-of-plane electric field occurs just near the areas of the accumulated charge. Note that in the case of the particle antenna, the measured spatial distribution of the loss probability corresponds to the out-of-plane electric field distribution of the particle antenna, which is close to the accumulated charge distribution in the particle antenna. In the case of the inverted aperture antenna, it corresponds to the out-of-plane electric field distribution, which is close to out-of-plane magnetic field distribution related to the particle antenna.

bow-tie, the highest loss probability is detected in the corners of the structure, where the charge is accumulated. In the case of the inverted bow-tie (i.e. aperture), the Babinet's principle says that its out-of-plane electric field distribution is the same as the out-of-plane magnetic field distribution of the particle. As EELS detects the out-of-plane electric field, in principle, we indirectly detect the spatial distribution of out-of-plane magnetic field corresponding to the transverse dipole mode in the particle when inspecting the first peak in the case of the inverted bow-tie. This is perfectly confirmed by the schematic mode analysis presented in Figure 4.3.

The second peak in Figure 4.2 has the energy of 1.67 eV in the case of the bow-tie and 1.76 eV in the case of the inverted bow-tie, respectively. The spatial distribution of the loss probability at the energy of the second peak exhibits maximum in the gap of the bow-tie and therefore corresponds to a longitudinal dipole mode. Note that in our geometry the longitudinal length of each wing is shorter than their tranversal length. It is again a mixture of a bonding and an antibodning mode consisting of parallel and antiparallel alignment of the dipoles in both wings (Figure 4.3 shows the antibonding case). Their energy difference is also in this case so low that they are not distinguishable by EELS. In the case of the inverted bow-tie, the energy of this mode is similar. However, the spatial distribution is rather different and again corresponds to the spatial distribution of the out-of-plane magnetic field of this mode in the particle bow-tie.

The third peak in Figure 4.2 is detected at 1.95 eV in the case of the bow-tie and at 1.93 eV in the case of the inverted bow-tie, respectively. The spatial distribution of the loss probability at the energy of the third peak exhibits maxima in the middle of all edges of the bow-tie and corresponds to a higher order mode – the edge mode.

To explore the tunability of bow-tie and inverted bow-tie antennas, their size was scaled. A set of bow-tie and inverted bow-tie antennas with the total length from 200 nm to 1500 nm was studied by EELS. The investigation was focused on detection of the energy and spatial distribution of all three LSP modes (transverse dipole mode, longitudinal dipole mode, and edge mode) introduced in Figure 4.3. The transverse dipole mode is tunable in the respect size region from 0.3 eV to 1.4 eV and the longitudinal dipole mode is tunable in the respect size region from 0.6 eV to 2.0 eV in antennas under study. Consequently, both modes are easily tunable through the near-infrared and visible red spectral region. Moreover, larger antennas will support LSP resonances tunable in infrared region at energies which are hardly accessible by electron beam spectroscopy.

4.3 Diabolo and inverted diabolo antennas

A typical diabolo antenna with the total length of 300 nm and a typical inverted diabolo antenna with the total length of 280 nm are shown in Figure 4.4. EEL spectra recorded at different positions reveal four distinct peaks. The nature of modes corresponding to these four peaks is revealed in loss probability maps at peak energies shown in Figure 4.5.

The first peak in Figure 4.4 is detected at 0.69 eV in the case of diabolo and at 0.73 eV in the case of inverted diabolo, respectively. The spatial distribution of the loss probability at the energy of the first peak exhibits maxima at the outer edges of the diabolo and therefore corresponds to a longitudinal dipole mode. If the diabolo is considered as a coupled structure consisting of two wings connected by a bridge, this mode corresponds to the longitudinal bonding dipole mode as the dipoles in both wings are oriented parallel and acts together to form the basic mode of the diabolo antenna. In the case of the inverted diabolo, the energy of this mode is similar. However, the spatial distribution is

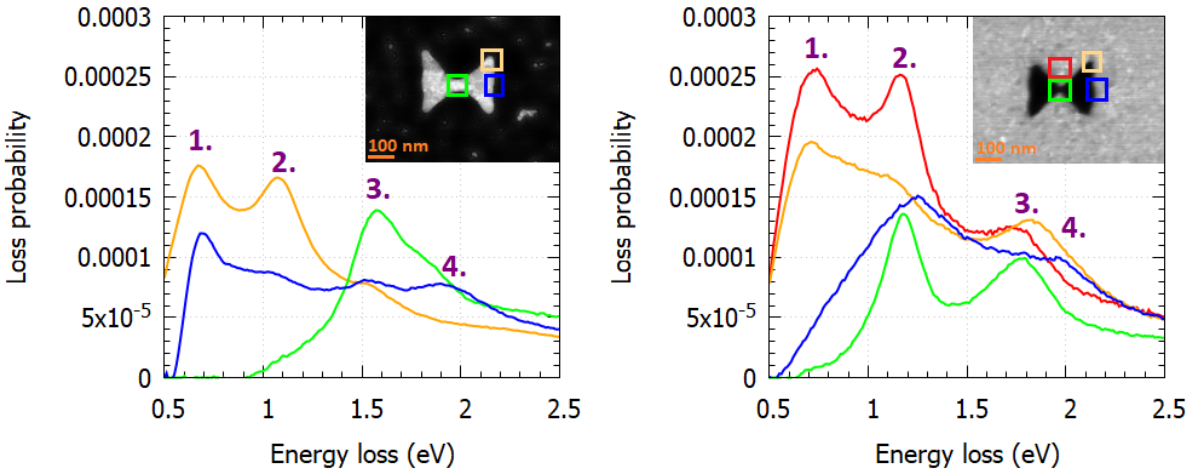

Figure 4.4: Background and ZLP subtracted normalized EEL spectra measured in the corner (orange), in the neck (green), next to the neck (red), and on the outer edge (blue) of the diabolo (left) and the inverted diabolo (right) antenna. The color squares in the insets indicate the areas where the respective spectra were collected. The first peak corresponds to the longitudinal bonding dipole mode, the second one to the transverse dipole mode, the third one to the longitudinal antibonding dipole mode, and the fourth one to the edge mode. For better description of these modes see Figure 4.5.

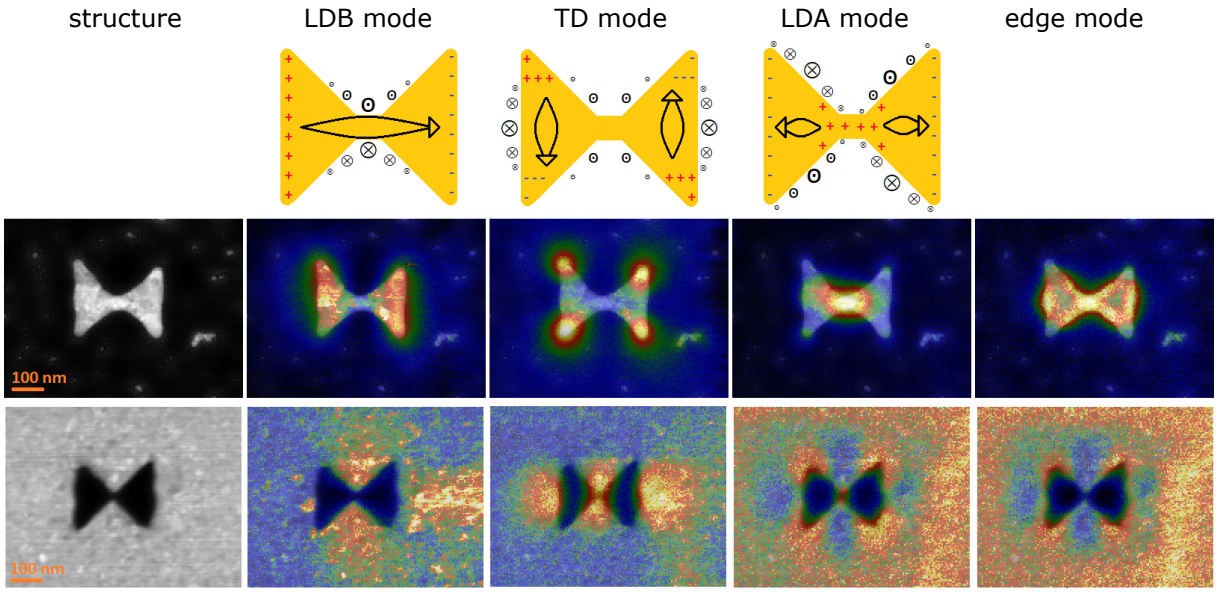

Figure 4.5: Schematic representation of detected plasmonic modes in the diabolo antenna followed by experimental data corresponding to the longitudinal bonding dipole (LDB) mode, the transverse dipole (TD) mode, the longitudinal antibonding dipole (LDA) mode, and the edge mode represented by the loss probability maps at the peak energies determined from Figure 4.4 placed over a shadow of the micrograph of the antenna shown in the left column. From the Gauss law it follows that the strongest out-of-plane electric field occurs just near the areas of the accumulated charge. Note that in the case of the particle antenna, the measured spatial distribution of the loss probability corresponds to the out-of-plane electric field distribution of the particle antenna, which is close to the accumulated charge distribution in the particle antenna. In the case of the inverted aperture antenna, it corresponds to out-of-plane electric field distribution of the aperture antenna, which is close to the out-of-plane magnetic field distribution of the particle antenna.

rather different. From the Gauss law it follows that the strongest out-of-plane electric field, detected by EELS, occurs just near the areas of the accumulated charge. Therefore, in the case of the particle bow-tie, the highest loss probability is detected in the corners of the structure, where the charge is accumulated. In the case of the inverted bow-tie (i.e. aperture), Babinet's principle says that the out-of-plane magnetic field of the particle has the same spatial distribution as the out-of-plane electric field of the aperture. As EELS detects the out-of-plane electric field, in principle, we detect the spatial distribution of the out-of-plane magnetic field corresponding to the longitudinal dipole mode in the particle when inspecting the first peak in the case of the inverted diabolo. This is perfectly confirmed by the schematic mode analysis presented in Figure 4.5. Note that we observe the same effect as in the case of the bow-tie and the inverted bow-tie discussed in Section 4.2.

The second peak in Figure 4.4 is detected at 1.09 eV in the case of the diabolo and at 1.18 eV in the case of the inverted diabolo, respectively. The spatial distribution of the loss probability at the energy of the second peak exhibits maxima in the corners of the diabolo antenna and therefore corresponds to a transverse dipole mode. It is a mixture of the bonding and the antibonding mode consisting of a parallel and an antiparallel alignment of the dipoles in both wings (Figure 4.5 shows the antibonding case). Their energy difference is in this case so low that they are not distinguishable by EELS. In the case of the inverted bow-tie, the energy of this mode is similar. The spatial distribution is rather different and corresponds to the spatial distribution of the out-of-plane magnetic field of this mode in the diabolo as expected (see Figure 4.5).

The third peak in Figure 4.4 has the energy of 1.58 eV in the case of diabolo and 1.83 eV in the case of inverted diabolo. The spatial distribution of the loss probability at the energy of the third peak exhibits a maximum in the neck of the diabolo and therefore corresponds to a longitudinal antibonding dipole mode where the dipoles in two wings are oriented antiparallel. Note that contrariwise to the bow-tie, the longitudinal bonding dipole mode and the longitudinal antibonding dipole mode are in the case of the diabolo well separated in energy and easily distinguished by EELS.

The fourth peak in Figure 4.4 is detected at 1.95 eV in the case of the diabolo and at 2.00 eV in the case of the inverted diabolo. The spatial distribution of the loss probability at the energy of the fourth peak exhibitss maxima in the middle of all edges of the diabolo and corresponds to a higher order mode – the edge mode.

To explore the tunability of diabolo and inverted diabolo antennas, their size was scaled. A set of diabolo and inverted diabolo antennas with the total length ranging from 200 nm to 750 nm was studied by EELS. The shortest length is the same as in the case of bow-tie antennas as even smaller structures would be rather difficult to fabricate. The longest length is half of the bow-tie longest length. Note that due to the presence of the conductive bridge the effective length in the longitudinal direction is different for the diabolo and bow-tie antenna. In the case of the diabolo antennas, it corresponds to the total length of the diabolo, whereas the effective length of the bow-tie corresponds to the half of the total length of the bow-tie. The investigation was focused on detection of the energy and spatial distribution of all four LSP modes (longitudinal bonding dipole mode, transverse dipole mode, longitudinal antibonding dipole mode, and edge mode) introduced in Figure 4.5. For the considered range of dimensions, the energy of the longitudinal bonding dipole mode is tunable from 0.3 eV to 1.0 eV, the transverse dipole mode is tunable from 0.6 eV to 1.5 eV, and the longitudinal antibonding dipole mode is tunable from 1.0 eV to 2.0 eV. Consequently, all the three modes are easily tunable through the near-infrared spectral region while the longitudinal antibonding dipole mode

is tunable in the visible red spectral region, too.

4.4 Comparison of all four types of the antennas

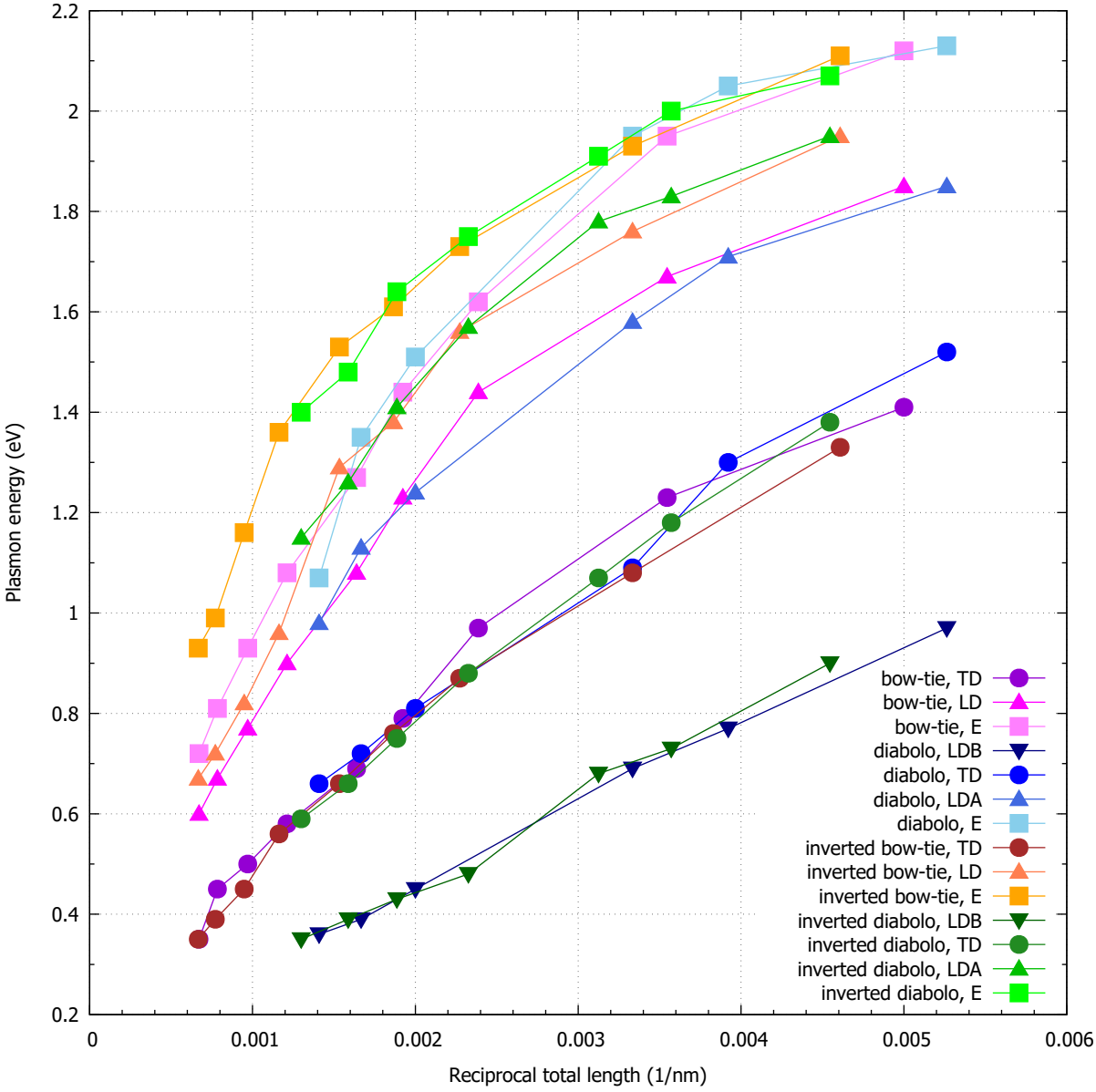

Figure 4.6: Dispersion relation showing the energies of plasmon modes as functions of reciprocal total length of the antenna for all discussed plasmon modes (longitudinal dipole bonding – LDB, transverse dipole – TD, longitudinal dipole antibonding – LDA or longitudinal dipole – LD, and quadrupole – Q) in all presented plasmonic antennas.

We can compare the spatial maps of the loss probability for all detected LSP modes in Figures 4.3 and 4.5. The size of the antennas is identical with respect to the fabrication uncertainty: the total length varies between 280 nm and 300 nm. The duality between bow-tie and diabolo antennas is clearly observed. The modes that do not involve charge transfer through the bridge of the antenna (transverse dipole, longitudinal dipole antibonding or longitudinal dipole, and edge) have identical spatial distribution of the loss probability in both direct and inverted structures. They also have similar mode energies.

The only difference is the longitudinal dipole bonding mode that includes charge transfer through the conductive bridge of diabolo antennas. Note that the diabolo antenna has the longitudinal dipole bonding mode well separated from the longitudinal dipole antibonding mode, whereas in the case of a bow-tie antenna these two modes are overlapping with each other. The same duality holds for the direct antennas as well as for the inverted antennas: the inverted bow-tie and inverted diabolo pair.

Figure 4.6 compares the energy of all detected LSP modes in all the four types of the antennas in the form of dispersion relations, where the plasmon energy is plotted as a function of the reciprocal total length of the antenna. This easily allows to compare the plasmon energy of modes in the antennas of a different total length. It can be seen, that the corresponding modes in all the four types of the antennas have the same energy. The best agreement is observed for the transverse dipole mode.

To sum up, the corresponding modes in the direct and inverted antennas, despite having identical energy, strongly differ in the spatial distribution of measured loss probability or the out-of-plane electric near fields.

4.5 Conclusion

To conclude, I have summarized the independent engineering of individual LSP modes in composite plasmonic antennas based on varying the coupling between the components via the insulating gap or the conductive bridge. LSP modes in bow-tie and diabolo antennas and apertures were identified and their properties such as the origin of transverse and longitudinal dipole modes, the spatial distribution of the modes, their tunability through the near-infrared and visible red spectral region, and Babinet's complementarity between direct and inverted antennas were described. The corresponding modes in direct and inverted antennas, despite having identical energy, strongly differ in the spatial distribution of measured loss probability or the out-of-plane electric near fields.

5 Silver amalgam nanoparticles

Silver amalgam is one of the most suitable solid electrode materials in electroanalysis of various reducible organic and inorganic compounds. They include heavy metals, agrochemicals, colorants, drugs, environmental pollutants, or biologically important compounds such as DNA, proteins and their constituents, and vitamins. The main advantage of silver amalgam within this context is its wide cathodic potential window, high mechanical stability, adequate sensitivity, and advantageous strong interaction with biopolymers (e.g. DNA and proteins) [105]. Nanostructuring the amalgam promises improved electrochemical performance and brings along the prospect of plasmonic activity. However, currently there is a lack of knowledge about the optical properties of nanostructured or even bulk silver amalgam which prevents its using in spectroelectrochemical and photochemical studies. In this chapter, a study of optical properties of silver amalgam and the plasmonic nature of its nanoparticles by analytical electron microscopy is presented.

5.1 Methods

Silver amalgam nanoparticles were prepared by chemical synthesis on indium-tin-oxide (ITO) substrates [105]. To prepare the sample for transmission electron microscopy, the silver amalgam nanoparticles were washed off the ITO into demineralized water in an ultrasonic bath. A few microliters of this suspension was dropped onto a silicon nitride membrane and dried. We used a standard 30 nm thick silicon nitride membrane for TEM with the window size of $250 \times 250\,\mu m^2$ and frame thickness of 200 µm by Agar Scientific.

TEM measurements were performed with the TEM FEI Titan equipped with the GIF Quantum spectrometer for electron energy loss spectroscopy (EELS) and the Super-X spectrometer for Energy dispersive X-ray spectroscopy (EDS) operated at 300 kV. For the spectroscopy measurements, a monochromated scanning regime was used, the beam current was set to 0.4 nA, and the FWHM of the ZLP was around 0.13 eV. In the case of EELS, we set convergence angle to 10 mrad, collection angle to 6.6 mrad, and dispersion of the GIF to 0.01 eV/pixel. We recorded EELS spectrum images with the pixel size of 3 nm. At every pixel, 10 cross-correlated EEL spectra with the acquisition time of 0.4 ms per spectrum were taken. The EEL spectra presented in this chapter were obtained by integrating the recorded signal over several pixels in the region of interest, ZLP and background subtracted, and divided by the integral intensity of the whole spectrum to transform measured counts to a quantity proportional to the loss probability. EEL maps show the EEL intensity at the plasmon peak energy integrated over the energy window of 0.2 eV. In the case of EDS, we integrated approximately 100 EDS spectrum images with the acquisition time of 10 µs per pixel. Spectrum images were post processed in the Velox software. The EDS quantification in weight percents was performed in this software using a parabolic background model and Brown-Powell ionization cross-section model.

Numerical simulations of EELS spectra were performed using the MNPBEM toolbox

[88, 89] based on the boundary element method (BEM). The dielectric function of the thick silver amalgam film was measured using spectroscopic ellipsometry [79] and the dielectric function of the silicon nitride membrane was set to 4 [91]. For the calculations of spectra and surface charge distribution, the electron beam was positioned 20 nm from the outer side of the antenna. The obtained loss probability density was recalculated to the loss probability at 0.01 eV energy intervals (corresponding to the dispersion of the spectrometer in the experiment).

5.2 Results

The chemical composition of a silver amalgam nanoparticle measured by STEM EDS is shown in Figure 5.1. The composition is rather homogeneous and reads in weight percents (54 ± 4) % of Ag and (46 ± 6) % of Hg. Next to the silver amalgam nanoparticle some small silver nanoparticles are located with the composition in weight percents reading (89 ± 4) % of Ag and (11 ± 4) % of Hg. Elemental maps of Si and N are homogenous and correspond to the signal generated by the silicon nitride membrane.

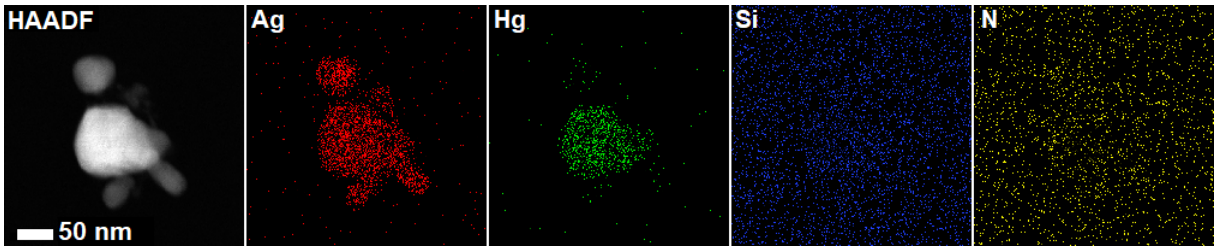

Figure 5.1: STEM HAADF micrograph of the silver amalgam nanoparticle with small silver nanoparticles around followed by the elemental maps showing the composition in weight percents of Ag and Hg constituting the nanoparticles together with Si and N from the membrane.

The simplest shape of an silver amalgam nanoparticle found on the sample was approximated by a disc with the diameter of 175 nm and the thickness of 80 nm. This particle was studied by EELS complemented by numerical simulations to describe the LSP resonances (Figure 5.2). The silver amalgam disc-shaped nanoparticle exhibits two peaks in the EEL spectrum. The first peak at 1.65 eV corresponds to the dipole LSP mode in the structure and the agreement between the experiment and the theory represented by the BEM simulation is excellent. The second peak at 3.5 eV in the experiment and at 3.25 eV in the theory represented by the BEM simulation show good agreement between the experiment and the theory. The difference between the experiment and the theory can be attributed to dielectric functions of silver amalgam and silicon nitride used in simulations as well as to the difference between the real shape of the particle and its idealized disc model. Note that the energy of the quadrupole mode in Figure 5.2 is approximately two times the energy of the dipole mode.

An important thing for potential application is the spectral range which can be covered by these silver amalgam nanoparticles. Figure 5.3 shows the dependency of the energy corresponding to the dipole LSP mode as a function of the particle size. First, the theoretical model represented by BEM simulation of a series of silver amalgam nanoparticles on a 30 nm thick silicon nitride membrane was performed. In total, six simulations were performed to cover the whole range of sizes and shapes close to the nanoparticles measured by EELS. The energy of the dipole LSP mode covers the whole visible range from 0.84 eV for the largest (400 nm) structure, which is already in the near-infrared region, to

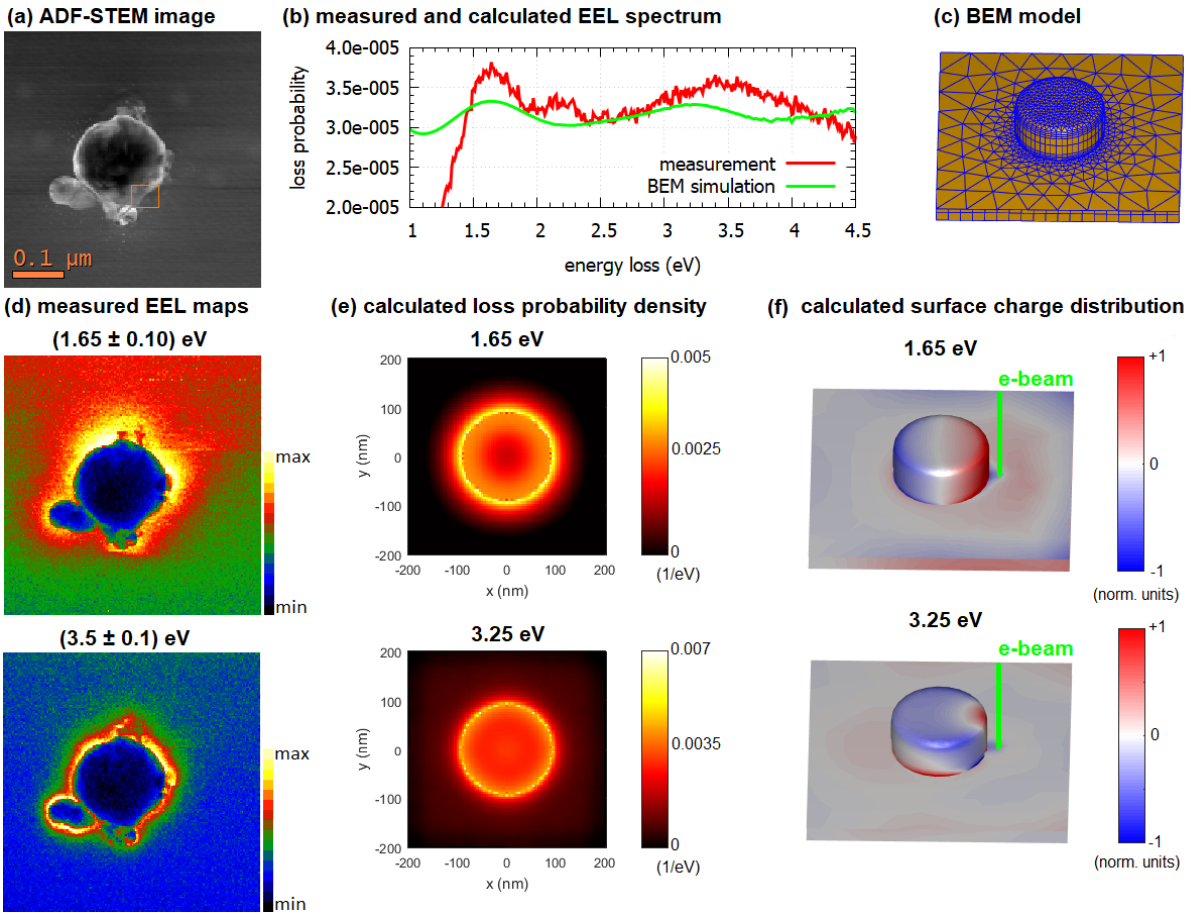

Figure 5.2: Silver amalgam nanoparticle approximated by a disc with the diameter of 175 nm and the thickness of 80 nm: (a) STEM ADF micrograph, (b) ZLP and background subtracted EEL spectrum integrated over the orange square in (a) complemented by numerical simulation, (c) simulation model of the disc with the mesh of boundary elements, (d) measured EEL maps at the energy of the peaks in (b), (e) calculated EEL maps at the energy of the peaks in (b), and (f) calculated surface charge distribution at the energy of the peaks in (b) clearly showing that the first peak corresponds to the dipole mode.

3.7 eV for the smallest (30 nm) structure, which is already in the ultraviolet region. Larger structures then support LSP resonances in the mid-infrared range. Second, this range was proved experimentally. A set of silver amalgam nanoparticles of a disc-like and a rod-like shape with their characteristic size ranging from 30 nm to 470 nm was measured by EELS (Figure 5.3b). In the case of the smallest rod like particle, the longitudinal dipole mode was not detected, but the transverse dipole mode at the energy of 3.7 eV corresponding to a characteristic size of 30 nm was measured. The disc with the diameter of 120 nm supports the dipole mode at 2.15 eV. The rod like particles with a length of 160 nm, 170 nm, 180 nm, 240 nm, and 470 nm support their longitudinal dipole mode at 1.82 eV, 1.77 eV, 1.65 eV, 1.35 eV, and 0.85 eV. Therefore, the measured dipole LSP resonances covered the whole visible range with an overlap to ultraviolet and near-infrared region. It should be noticed, that larger structures, which are not optimal for EELS measurements with our TEM microscope, have their resonances in the mid-infrared region [79]. The agreement between the simulation and the experiment is reasonably good.

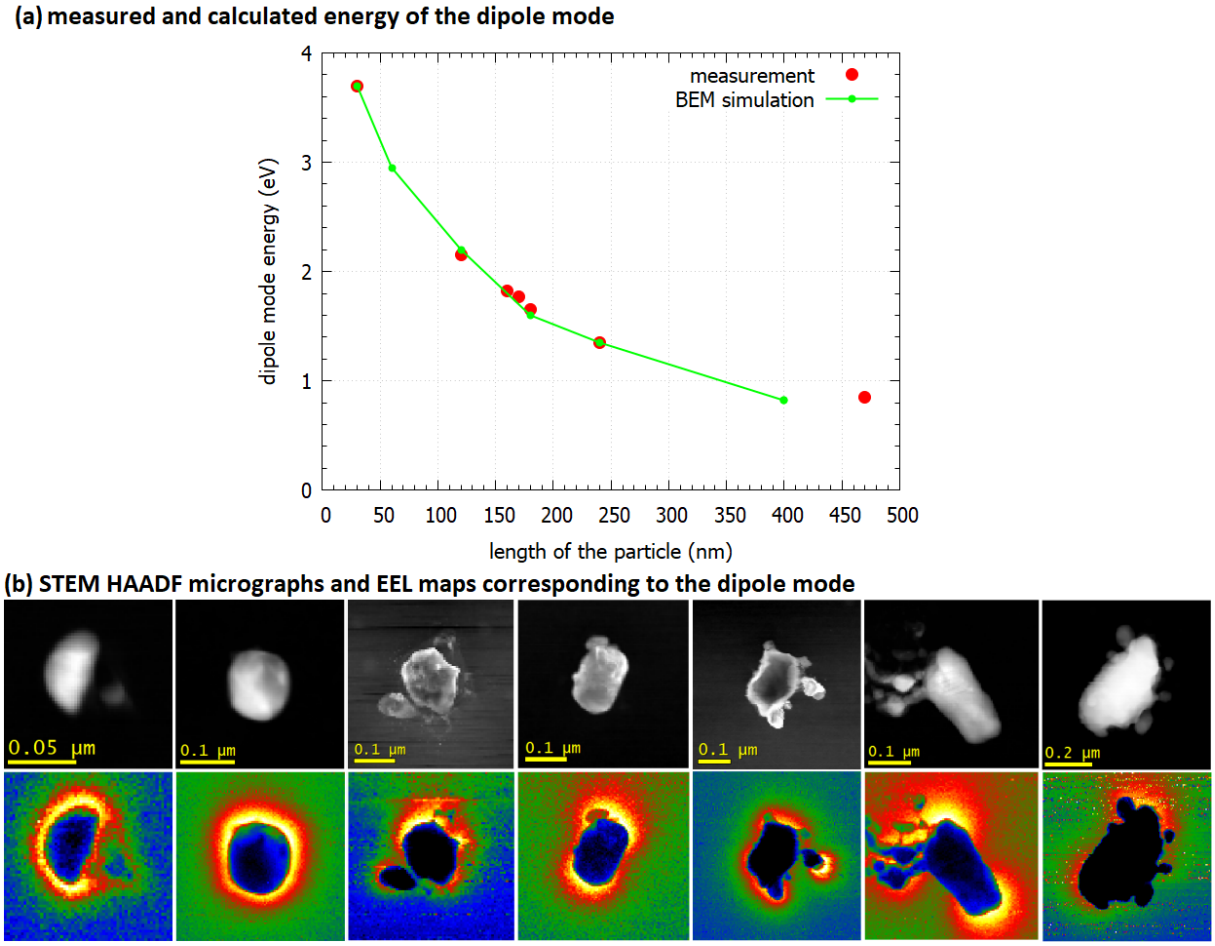

Figure 5.3: Silver amalgam nanoparticles of different sizes: (a) measured and calculated energy corresponding to the dipole mode, (b) STEM HAADF micrographs of silver amalgam nanoparticles with their characteristic size from 30 nm to 470 nm and measured EEL maps at the energy corresponding to their dipole mode.

5.3 Conclusion

To conclude, silver amalgam is a novel and very promising plasmonic material. By changing the size of nanostructures the dipole LSP resonance can be tuned from ultraviolet through the whole visible to infrared region. A minor disadvantage is the absorption in the silver amalgam itself as the imaginary part of its dielectric function reaches rather high values in the visible region. The main advantage is that silver amalgam is well investigated in the field of electrochemistry so the silver amalgam nanoparticles opens a possibility to combine plasmonics and electrochemistry together.

6 Conclusion

To summarize, this thesis was focused on electron and ion beam techniques for fabrication and characterization of plasmonic nanostructures. Analytical electron microscopy was discussed focusing on applications in the field of plasmonics. The emphasis was given to electron energy loss spectroscopy (EELS) and cathodoluminescence. Fabrication of plasmonic samples for transmission electron microscopy was introduced while the focus was given to focused ion beam lithography and to sample preparation using chemically synthesized particles in water solution. This thesis had four main research results.

The first result is a comparative study of plasmonic antennas fabricated by electron beam and focused ion beam lithography. While both techniques are suitable for the fabrication of plasmonic antennas, electron beam lithography shall be prioritized over focused ion beam lithography due to better quality of the resulting antennas and considerably stronger plasmonic response in EELS. Antennas fabricated by focused ion beam lithography have slightly dull edges, exhibit pronounced thickness fluctuation, and they are also strongly contaminated not only by organic contaminants, but also by residues of FIB milling including implanted milling ions and atoms of the titanium adhesion layer.

The second result is a study of Babinet's principle of complementarity for gold disc-shaped plasmonic antennas. The emphasis was given on experimental study using spatially-resolved EELS and cathodoluminescence to investigate the electromagnetic response of elementary plasmonic antennas: gold discs and complementary disc-shaped apertures in a gold layer prepared by focused ion beam lithoghraphy. I have experimentally verified that solid and hollow disc-shaped plasmonic antennas exhibit Babinet's complementarity. The complementarity was confirmed for fundamental plasmon properties such as resonance energies, but differences rising from the limited validity of Babinet's principle were found, for example, for the spatial distribution of the near-field of plasmon polaritons. Observed differences were from the practical point of view rather minor. The validity of Babinet's principle is relevant also for numerous applications. Babinet's complementarity allows to toggle between the magnetic and electric response, or between the reflection and transmission mode. While particles have to be supported by the substrate, substrate-less apertures self-supported by their frame can be fabricated. Apertures also offer better heat and charge management as the thin metallic film surrounding the apertures is usually a better conductor than the substrate supporting the particles.

The third result is the independent engineering of individual localized surface plasmon modes in composite plasmonic antennas based on varying the coupling between the components via insulating gap or conductive bridge together with Babinet's principle of complementarity. I have studied bow-tie and diabolo plasmonic antennas, both in the form of particles and in the form of apertures, which exhibit particularly strong local field enhancement. I have identified several modes of localized surface plasmons in these antennas and characterize their properties including mode energy, near field electric and magnetic field distribution, and the qualitative distribution of charge nodes and current

associated with electron gas oscillations. I have studied mode energy tunability in near infrared and visible spectral regions and Babinet's complementarity between direct and inverted antennas. The corresponding modes in direct and inverted antennas, despite having identical energy, strongly differ in the spatial distribution of measured loss probability or the out-of-plane electric near fields, respectively. From the Gauss law it follows that the strongest out-of-plane electric field occurs just near the areas of the accumulated charge. Note that the measured spatial distribution of the loss probability corresponds, in the case of a particle antenna, to the out-of-plane electric field distribution in this antenna, which is close to the accumulated charge distribution of the particle antenna. In the case of an inverted aperture antenna, it corresponds to the out-of-plane electric field distribution of the aperture antenna, which is close to the out-of-plane magnetic field distribution of the particle antenna.

The fourth result is the characterization of a novel plasmonic material – silver amalgam. I have studied nanparticles made of silver amalgam. I have experimentally proved that by changing the size of nanostructures the dipole localized surface plasmon resonance can be tuned through the whole visible and infrared region. A minor disadvantage is the absorption in the silver amalgam itself as the imaginary part of its dielectric function reaches rather high values in the visible region. The main advantage is that silver amalgam is well investigated in the field of electrochemistry so the silver amalgam nanoparticles opens a possibility to combine plasmonics and electrochemistry together.

To conclude, in this Thesis I have introduced the application of analytical electron microscopy in the field of plasmonics covering both the fabrication and characterization processes. I have fully covered all five main aims: (i) to introduce analytical electron microscopy and its prospective for plasmonics and to give a brief overview of fabrication of plasmonic antennas for electron beam spectroscopy investigations focused on focused ion beam lithoghraphy, (ii) to investigate elementary gold plasmonic antennas with focus on Babinet's principle of complementarity, (iii) to study nanostructures with functional properties related to the local enhancement of electric and magnetic field, (iv) to explore the possibility of fabrication of plasmonic antennas using based on a frequently used material, and (v) to study coupled structures. Finally, my work have contributed to the publication of several manuscripts, and paved the way for a wide use of presented techniques at CEITEC BUT in the future.

Further research in this field may deal, for example, with the following topics. Gold can be replaced by another metal, for example, aluminum or silver to extend the available energy range to the whole visible region. This would be necessary to explore the EELS and CL complementarity more accurately. Second, the strong coupling phenomena with the substrate is observed in the infrared range, which was not accessible by available analytical transmission electron microscopes as it requires either an ultra high energy resolution EELS, or CL spectrometer designed for the respect infrared spectral region. However, it is not impossible to measure it in the near future in a laboratory with a suitable microscope. Another possibility is to use phase shaped electron beams for EELS or cathodoluminescence. To summarize, analytical electron microscopy in plasmonics will deal with many interesting topics in the future.

References

[1] Novotny, L., Hecht, B.: *Principles of Nano-Optics*. Cambridge Press New York, 2006, 539 p. ISBN 978-0-521-83224-3.

[2] Ritchie, R. H.: Plasma losses by fast electrons in thin films. *Physical Review*, vol. 106, 1957, p. 874.

[3] Powell, C. J., Swan, J. B.: Effect of oxidation on the characteristic loss spectra of aluminum and magnesium. *Physical Review*, vol. 118, 1960, p. 640.

[4] Otto, A.: Theory of plasmon excitation in thin films by electrons. *Physica status solidi*, vol. 22, 1967, p. 401.

[5] Lucas, A. A., Šunjič, M.: Fast-electron spectroscopy of surface excitations. *Physical Review Letters*, vol. 26, 1971, p. 229.

[6] Kröger, E.: Berechnung der Energieverluste schneller Elektronen in dünnen Schichten mit Retardierung. *Zeitschrift für Physik*, vol. 216, 1968, p. 115.

[7] Kröger, E.: Transition radiation, Cerenkov radiation and energy losses of relativistic charged particles traversing thin foils at oblique incidence. *Zeitschrift für Physik*, vol. 235, 1970, p. 403.

[8] Maier, S. A.: *Plasmonics: Fundamentals and Applications*. Springer Science+Business Media LLC New York, 2007. ISBN 978-0387-33150-8.

[9] Mie, G.: Beiträge zur Optik trüber Medien, speziell kolloidaler Metallösungen. *Annalen der Physik*, vol. 25, 1908, p. 377.

[10] Batson, P. E.: Surface plasmon coupling in clusters of small spheres. *Physical Review Letters*, vol. 49, 1982, p. 1682.

[11] Schuller, J. A., *et al.*: Plasmonics for extreme light concentration and manipulation. *Nature Materials*, vol. 9, 2010, p. 193.

[12] Kelly, K. L., *et al.*: The optical properties of metal nanoparticles: The influence of size, shape, and dielectric environment. *Journal of Physical Chemistry B*, vol. 107, 2003, p. 668.

[13] Stockman, M. I.: Nanoplasmonics: The physics behind the applications. *Physics Today*, vol. 64, 2011, p. 39.

[14] Stockman, M. I., *et al.*: Roadmap on plasmonics. *Journal of Optics*, vol. 20, 2018, p. 043001.

[15] Salerno, M., *et al.*: Plasmon polaritons in metal nanostructures: The optoelectronic route to nanotechnology. *Opto-Electronics Review*, vol. 10, 2002, p. 217.

[16] Mattiucci, N., D'Aguanno, G., Bloemer, M. J.: Long range plasmon assisted all-optical switching at telecommunication wavelengths. *Optics Letters*, vol. 37, 2012, p.121.

[17] Knight, M. W., *et al.*: Photodetection with active optical antennas. *Science*, vol. 332, 2011, p. 702.

[18] Smolyaninov, I. I., *et al.*: Far-field optical microscopy with a nanometer-scale resolution based on the in-plane image magnification by surface plasmon polaritons. *Physical Review Letters*, vol. 94, 2005, p. 057401.

[19] Willets, K. A., Van Duyne, R. P.: Localized surface plasmon resonance spectroscopy and sensing. *Annual Review of Physical Chemistry*, vol. 58, 2007, p. 267.

[20] Boriskina, S. V., Ghasemi, H., Chen, G.: Plasmonic materials for energy: From physics to applications. *Materials Today*, vol. 16, 2013, p. 375.

[21] Aćimović, S. S., *et al.*: LSPR chip for parallel, rapid, and sensitive detection of cancer markers in serum. *Nano Letters*, vol. 14, 2014, p. 2636.

[22] Baffou, G., Quidant, R.: Thermo-plasmonics: Using metallic nanostructures as nanosources of heat. *Laser & Photonic Review*, vol. 7, 2013, p. 171.

[23] Sheldon, M. T., *et al.*: Plasmoelectric potentials in metal nanostructures. *Science* vol. 346, 2014, p. 828.

[24] Zheludev, N. I., *et al.*: Lasing spaser. *Nature Photonics*, vol. 2, 2008, p. 351.

[25] Yu, N., *et al.*: Light propagation with phase discontinuities: generalized laws of reflection and refraction. *Science* vol. 334, 2011, p. 333.

[26] Cardano, F., Marrucci, L.: Spin–orbit photonics. *Nature Photonics*, vol. 9, 2015, p. 776.

[27] Valev, V. K., *et al.*: Chirality and chiroptical effects in plasmonic nanostructures: fundamentals, recent progress, and outlook. *Advanced Materials*, vol. 25, 2013, p. 2517.

[28] Falcone, F., *et al.*: Babinet principle applied to the design of metasurfaces and metamaterials. *Physical Review Letters*, vol. 93, 2004, p. 197401.

[29] Zentgraf, T., *et al.*: Babinet's principle for optical frequency metamaterials and nanoantennas *Physical Review B*, vol. 76, 2007, p. 033407.

[30] Ferrando, R., Jellinek, J., Johnston, R. L.: Nanoalloys: From theory to applications of alloy clusters and nanoparticles. *Chemical Reviews*, vol. 108, 2008, p. 845.

[31] Kunkemöller, G., *et al.*: Extreme ultraviolet proximity lithography for fast, flexible and parallel fabrication of infrared antennas. *Optics Express*, vol. 23, 2015, p. 25487.

[32] Vieu, C., *et al.*: Electron beam lithography: resolution limits and applications. *Applied Surface Science*, vol. 164, 2000, p. 111.

[33] Taylor, A. B., *et al.*: Electron-beam lithography of plasmonic nanorod arrays for multilayered optical storage. *Optics Express*, vol. 22, 2014, p. 13234.

[34] Joshi-Imre, A., Bauerdick, S.: Direct-write ion beam lithography. *Journal of Nanotechnology*, vol. 2014, 2014, p. 170415.

[35] Kollmann, H., *et al.*: Toward plasmonics with nanometer precision: nonlinear optics of helium-ion milled gold nanoantennas. *Nano Letters*, vol. 14, 2014, p. 4778.

[36] Winkler, R., *et al.*: Direct-write 3D nanoprinting of plasmonic structures. *ACS Applied Materials & Interfaces*, vol. 9, 2017, p. 8233.

[37] Winkler, R., *et al.*: High-fidelity 3D-nanoprinting via focused electron beams: growth fundamentals. *ACS Appllied Nano Materials*, vol. 1, 2018, p. 1014.

[38] Knight, M. W., *et al.*: Aluminum for Plasmonics. *ACS Nano*, vol. 8, 2014, p. 834.

[39] King, N. S., *et al.*: Fano resonant aluminum nanoclusters for plasmonic colorimetric sensing. *ACS Nano*, vol. 9, 2015, p. 10628.

[40] Cheng, F., *et al.*: Aluminum plasmonic metamaterials for structural color printing. *Optics Express*, vol. 23, 2015, p. 14552.

[41] Madsen, S. J., *et al.*: Observing plasmon damping due to adhesion layers in gold nanostructures using electron energy loss spectroscopy. *ACS Photonics*, vol. 4, 2017, p. 268.

[42] Habteyes, T. G., *et al.*: Metallic adhesion layer induced plasmon damping and molecular linker as a nondamping alternative. *ACS Nano*, vol. 6, 2012, p. 5702.

[43] Tinguely, J. C., *et al.*: Gold nanoparticles for plasmonic biosensing: the role of metal crystallinity and nanoscale roughness. *BioNanoScience*, vol. 1, 2011, p. 128.

[44] Bosman, M., *et al.*: Encapsulated annealing: enhancing the plasmon quality factor in lithographically-defined nanostructures. *Scientific Reports*, vol. 4, 2014, p. 5537.

[45] Rodríguez-Fernández, J., *et al.*: The effect of surface roughness on the plasmonic response of individual sub-micron gold spheres. *Physical Chemistry Chemical Physics*, vol. 11, 2009, p. 5909.

[46] Trügler, A., *et al.*: Influence of surface roughness on the optical properties of plasmonic nanoparticles. *Physical Review B*, vol. 83, 2011, p. 081412.

[47] Hu, M., *et al.*: Dark-field microscopy studies of single metal nanoparticles: understanding the factors that influence the linewidth of the localized surface plasmon resonance. *Journal of materials chemistry*, vol. 18, 2008, p. 1949.

[48] Cao, W., *et al.*: Localized surface plasmon resonance of single silver nanoparticles studied by dark-field optical microscopy and spectroscopy. *Journal of Applied Physics*, vol. 109, 2011, p. 034310.

[49] Ashino, M., Ohtsu, M.: Fabrication and evaluation of a localized plasmon resonance probe for near-field optical microscopy/spectroscopy. *Applied Physics Letters*, vol. 72, 1998, p. 1299.

[50] Vasconcelos, T. L., *et al.*: Tuning Localized Surface Plasmon Resonance in Scanning Near-Field Optical Microscopy Probes. *ACS Nano*, vol. 9, 2015, p. 6297.

[51] García de Abajo, F. J.: Optical excitations in electron microscopy. *Reviews of modern physics*, vol. 82, 2010, p. 209.

[52] Losquin, A., Lummen, T. T. A.: Electron microscopy methods for space-, energy-, and time-resolved plasmonics. *Frontiers of Physics*, vol. 12, 2017, p. 127301.

[53] Nelayah, J., *et al.*: Mapping surface plasmons on a single metallic nanoparticle. *Nature Physics*, vol. 3, 2007, p. 348.

[54] Colliex, C., Kociak, M., Stéphan, O.: Electron energy loss spectrometry imaging of surface plasmons at the nanometer scale. *Ultramicroscopy*, vol. 162, 2016, p. A1.

[55] Wu, Y., Li, G., Camden, J. P.: Probing nanoparticle plasmon with electron energy loss spectroscopy. *Chemical Reviews*, vol. 118, 2018, p. 2994.

[56] Nelayah, J., *et al.*: Direct imaging of surface plasmon resonances on single triangular silver nanoprisms at optical wavelength using low-loss EFTEM imaging. *Optics Letters*, vol. 34, 2009, p. 1003.

[57] Yamamoto, N., Araya, K., García de Abajo, F. J.: Photon emission from silver particles induced by a high-energy electron beam. *Physical Review B*, vol. 64, 2001, p. 205419.

[58] Yamamoto, N.: Development of high-resolution cathodoluminescence system for STEM and application to plasmonic nanostructures. *Microscopy*, vol. 65, 2016, p. 282.

[59] Sun, Q., *et al.*: Direct imaging of the near field and dynamics of surface plasmon resonance on gold nanostructures using photoemission electron microscopy. *Light: Science & Applications*, vol. 2, 2013, p. e118.

[60] Park, S. T., Lin, M., Zewail1, A. H.: Photon-induced near-field electron microscopy (PINEM): theoretical and experimental. *New Journal of Physics*, vol. 12, 2010, p. 123028.

[61] Asenjo-Garcia, A., García de Abajo, F. J.: Plasmon electron energy-gain spectroscopy. *New Journal of Physics*, vol. 15, 2013, p. 103021.

[62] Tizei, L.H.G., *et al.*: Monolayer and thin h-BN as substrates for electron spectro-microscopy analysis of plasmonic nanoparticles. *Applied Physics Letters*, vol. 113, 2018, p. 231108.

[63] Department of Solid State Physics and Surfaces, Brno University of Technology: *Plasmonics & Nanophotonics.* <http://surfaces.fme.vutbr.cz/research/plasmonics/>

[64] Babocký, J., *et al.*: Quantitative 3D phase imaging of plasmonic metasurfaces. *ACS Photonics*, vol. 4, 2017, p. 1389.

[65] Ligmajer, F., *et al.*: Epitaxial VO2 nanostructures: a route to large-scale, switchable dielectric metasurfaces. *ACS Photonics*, vol. 5, 2018, p. 2561.

[66] Dvořák, P., *et al.*: Control and near-field detection of surface plasmon interference patterns. *Nano Letters*, vol. 13, 2013, p. 2558.

[67] Dvořák, P., *et al.*: Imaging of near-field interference patterns by aperture-type SNOM – influence of illumination wavelength and polarization state. *Optics Express*, vol. 25, 2017, p. 16560.

[68] Dvořák, P., *et al.*: Near-field digital holography: a tool for plasmon phase imaging. *Nanoscale*, vol. 10, 2018, p. 21363.

[69] Bouchal, P., *et al.*: High-resolution quantitative phase imaging of plasmonic metasurfaces with sensitivity down to a single nanoantenna. *Nano Letters*, vol. 19, 2019, p. 1242.

[70] Křápek, V., *et al.*: Spatially resolved electron energy loss spectroscopy of crescent-shaped plasmonic antennas. *Optics Express*, vol. 23, 2015, p. 11855.

[71] Horák, M., *et al.*: Limits of Babinet's principle for solid and hollow plasmonic antennas. *Scientific Reports*, vol. 9, 2019, p. 4004.

[72] Babocký, J.: *Fabrication and characterization of nanostructures with functional properties in the field of plasmonics I.* Brno: Vysoké učení technické v Brně, Středoevropský technologický institut, 2019. Dizertační práce, vedoucí práce prof. RNDr. Tomáš Šikola, CSc.

[73] Babocký, J., *et al.*: Patterning large area plasmonic nanostructures on nonconductive substrates using variable pressure electron beam lithography. *Journal of Vacuum Science & Technology B*, vol. 34, 2016, p. 06K801.

[74] Šamořil, T.: *Aplikace fokusovaného iontového a elektronového svazku v nanotechnologiích.* Brno: Vysoké učení technické v Brně, Fakulta strojního inženýrství, 2015. 126 s. Dizertační práce, vedoucí práce prof. RNDr. Tomáš Šikola, CSc.

[75] Horák, M., *et al.*: Comparative study of plasmonic antennas fabricated by electron beam and focused ion beam lithography. *Scientific Reports*, vol. 8, 2018, p. 9640.

[76] Hrtoň, M., Křápek, V., Šikola, T.: Boundary element method for 2D materials and thin films. *Optics Express*, vol. 25, 2017, p. 23709.

[77] Břínek, L.: *Aplikace plazmonových polaritonů v nanofotonice.* Brno: Vysoké učení technické v Brně, Fakulta strojního inženýrství, 2015. 75 s. Dizertační práce, vedoucí práce Prof. RNDr. Petr Dub, CSc.

[78] Horák, M., Křápek, V., Šikola, T.: Plazmonové rezonance ve zlatých nanočásticích zkoumané s využitím elektronové mikroskopie. *Jemná Mechanika a Optika*, vol. 62, 2017, p. 303.

[79] Ligmajer, F., *et al.*: Silver amalgam nanoparticles: a novel plasmonic platform for spectro-electrochemistry. *Journal of Physical Chemistry C*, 2019.

[80] Křápek, V., *et al.*: Independent engineering of individual plasmon modes in plasmonic dimers with conductive and capacitive coupling. In preparation. *Arxiv preprint*, arxiv:1905.09210.

[81] Hrtoň, M., *et al.*: Plasmonic antennas with electric, magnetic, and electromagnetic hot spots based on Babinet's principle. In preparation. *Arxiv preprint*, arxiv:1904.01397.

[82] Duan, H., *et al.*: Metrology for electron-beam lithography and resist contrast at the sub-10 nm scale. *Journal of Vacuum Science & Technology B*, vol. 28, 2010, p. C6H11.

[83] Huang, J. S., *et al.*: Atomically flat single-crystalline gold nanostructures for plasmonic nanocircuitry. *Nature Communication*, vol. 1, 2010, p. 150.

[84] Wang, X., *et al.*: Vapor-phase preparation of single-crystalline thin gold microplates using $HAuCl_4$ as the precursor for plasmonic applications. *RSC Advances*, vol. 6, 2016, p. 74937.

[85] Postek, M. T.: An approach to the reduction of hydrocarbon contamination in the scanning electron microscope. *Scanning*, vol. 18, 1996, p. 269.

[86] Egerton, R. F., Li, P., Malac, M.: Radiation damage in the TEM and SEM. *Micron*, vol. 35, 2004, p. 399.

[87] Walczyk, W., Schön, P. M., Schönherr, H.: The effect of PeakForce tapping mode AFM imaging on the apparent shape of surface nanobubbles. *Journal of Physics: Condensed Matter*, vol. 25, 2013, p. 1.

[88] Hohenester, U.: Simulating EELS with the MNPBEM toolbox. *Computer Physics Communications*, vol. 185, 2014, p. 1177.

[89] Waxenegger, J., Trügler, A., Hohenester, U.: Plasmonics simulations with the MNPBEM toolbox: Consideration of substrates and layer structures. *Computer Physics Communications*, vol. 193, 2015, p. 138.

[90] Olmon, R. L., *et al.*: Optical dielectric function of gold. *Physical Review B*, vol. 86, 2012, p. 235147.

[91] Schmidt, F. P., *et al.*: Morphing a plasmonic nanodisk into a nanotriangle. *Nano Letters*, vol. 14, 2014, p. 4810.

[92] Mitchell, D. R. G.: Determination of mean free path for energy loss and surface oxide film thickness using convergent beam electron diffraction and thickness mapping: a case study using Si and P91 steel. *Journal of Microscopy*, vol. 224, 2006, p. 187.

[93] Iakoubovskii, K., *et al.*: Thickness measurements with electron energy loss spectroscopy. *Microscopy Research and Technique*, vol. 71, 2008, p. 626.

[94] Michael, J. R.: Focused ion beam induced microstructural alterations: texture development, grain growth, and intermetallic formation. *Microscopy and Microanalysis*, vol. 17, 2011, p. 386.

[95] Schmidt, F. P., *et al.*: Dark plasmonic breathing modes in silver nanodisks. *Nano Letters*, vol. 12, 2012, p. 5780.

[96] Koh, A. L., *et al.*: Electron energy-loss spectroscopy (EELS) of surface plasmons in single silver nanoparticles and dimers: Influence of beam damage and mapping of dark modes. *ACS Nano*, vol. 3, 2009, p. 3015.

[97] Pyykkö, P., Atsumi, M.: Molecular single-bond covalent radii for elements 1–118. *Chemistry: A European Journal*, vol. 15, 2009, p. 186.

[98] Hentschel, M., *et al.*: Babinet to the half: coupling of solid and inverse plasmonic structures. *Nano Letters*, vol. 13, 2013, p. 4428.

[99] Johnson, P. B., Christy, R. W.: Optical constants of the noble metals. *Physical Review B*, vol. 6, 1972, p. 4370.

[100] Bitzer, A., *et al.*: Terahertz near-field microscopy of complementary planar metamaterials: Babinet's principle. *Optics Express*, vol. 19, 2001, p. 2537.

[101] Yang, H. U., *et al.*: Accessing the optical magnetic near-field through Babinet's principle. *ACS Photonics*, vol. 1, 2014, p. 894.

[102] Yacobi, B. G., Holt, D. B.: *Cathodoluminescence microscopy of inorganic solids.* Springer Science+Business Media New York, 1990. ISBN 978-1-4757-9595-0.

[103] Novotny, L., van Hulst, N.: Antennas for light. *Nature Photonics*, vol. 5, 2011, p. 83.

[104] Grosjean, T., *et al.*: Diabolo nanoantenna for enhancing and confining the magnetic optical field. *Nano Letters*, vol. 11, 2011, p. 1009.

[105] Daňhel, A., *et al.*: Electrodeposition of silver amalgam particles on ITO – Towards novel electrode material. *Journal of Electroanalytical Chemistry*, vol. 821, 2018, p. 53.